
RECOVER CELL TENSOR: DIFFUSION-EQUIVALENT TENSOR COMPLETION FOR FLUORESCENCE MICROSCOPY IMAGING

Chenwei Wang, Zhaoke Huang, Zelin Li, Wenqi Zhu
Hong Kong

Abstract

Fluorescence microscopy (FM) imaging is a fundamental technique for observing live cell division, one of the most essential processes in the cycle of life and death. Observing 3D live cells requires scanning through the cell volume while minimizing lethal phototoxicity. That limits acquisition time and results in sparsely sampled volumes with anisotropic resolution and high noise. Existing image restoration methods, primarily based on inverse problem modeling, assume known and stable degradation processes and struggle under such conditions, especially in the absence of high-quality reference volumes. In this paper, from a new perspective, we propose a novel tensor completion framework tailored to the nature of FM imaging, which inherently involves nonlinear signal degradation and incomplete observations. Specifically, FM imaging with equidistant Z-axis sampling is essentially a tensor completion task under a uniformly random sampling condition. On one hand, we derive the theoretical lower bound for exact cell tensor completion, validating the feasibility of accurately recovering 3D cell tensor. On the other hand, we reformulate the tensor completion problem as a mathematically equivalent score-based generative model. By incorporating structural consistency priors, the generative trajectory is effectively guided toward denoised and geometrically coherent reconstructions. Our method demonstrates state-of-the-art performance on SR-CACO-2 and three real *in vivo* cellular datasets, showing substantial improvements in both signal-to-noise ratio and structural fidelity.

1 Introduction

Cell division is one of the most fundamental processes of life—it drives growth and reproduction, yet also sets the stage for aging and death [1, 2, 3]. Observing the 3D membrane structure of cells during live cell division is essential for advancing biological research [4], which requires scanning through cell volume alone Z-axis with the aid of fluorescent dyes. To minimize lethal phototoxicity, the scanning time is strictly limited by XY-plane imaging at equidistant intervals along the Z-axis. As a result, 3D live-cell volume faces challenges like anisotropic resolution, and spatially varying noise, as illustrated in Fig. 1. These constraints significantly compromise the spatial-temporal resolution of live-cell volumetric imaging, thereby impeding fundamental insights in a wide range of biomedical fields [5, 3, 6].

Current most of image recovery algorithms are based on the inverse problem [7], which aims to model the degradation mapping even the the degradation process is unknown. As discussed in prior studies, many of these methods rely on supervised learning with known degradation models, requiring large paired datasets of high- and low-quality images, such as SRCNN [8], FSRCNN [9, 10], and DDPM [11]. These approaches are less suited to 3D fluorescence microscopy, where high-quality references are not available. To mitigate the reliance on paired data, unsupervised methods like CycleGAN [12], CinCGAN [13], and Deep Image Prior [14] have been proposed. Additionally, recent efforts using self-supervised learning [15, 16, 17] and transformer-based architectures [18, 19, 20, 21] have shown promise. A more detailed discussion of related work is provided in Appendix C.

However, FM imaging involves a nonlinear and complex imaging process influenced by excitation, fluorescence emission and sample heterogeneity [22, 23, 24]. This process is further complicated by high noise levels and

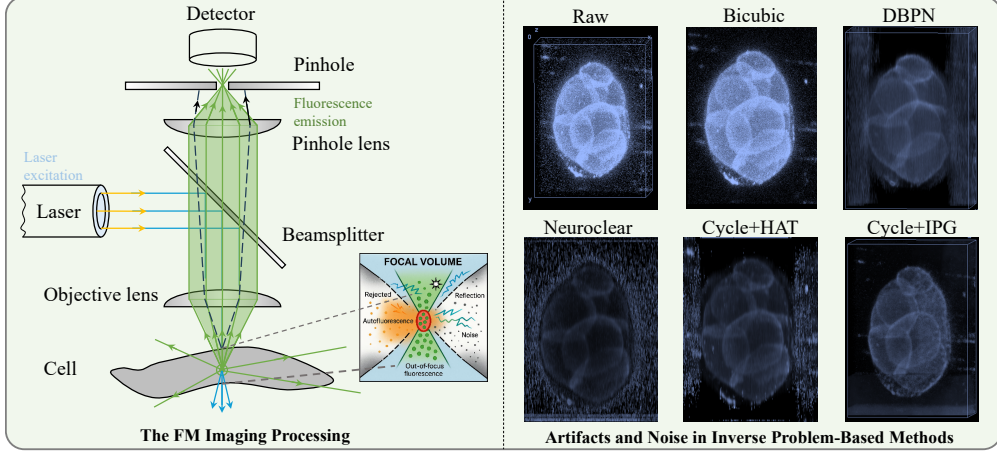


Figure 1: Illustration of the FM imaging process and comparison of reconstructed results across different methods. The schematic (left) shows the fluorescence imaging pipeline, where excitation light passes through optical components and interacts with the specimen before being detected. Raw observations are corrupted by noise and optical degradation. Reconstructed images using inverse-problem-based methods (e.g., IPG, CycleGAN) often suffer from hallucinated structures and residual noise.

incomplete signal acquisition due to attenuation and scattering. Traditional inverse problem methods, which rely on linear models and known physical assumptions [25, 26, 27, 7, 28], struggle to accurately capture the underlying core pattern of 3D live-cell with such complexity. Under noisy or incomplete conditions with equidistant Z-axis sampling, these methods often become ill-posed and produce unstable or ambiguous reconstructions [29, 30], as shown in Fig. 1, which limits their reliability for life science applications. The details are presented in Section 2.

In this paper, we first highlight that most image restoration approaches grounded in inverse problem formulations may adversely affect the accuracy and fidelity of 3D cell recovery. Then, we propose a cell tensor completion model, derive the cell-recovery bound and uncover its equivalence to a conditional diffusion framework to counter the evil. Specifically, our contributions are summarized as follows.

- From a new perspective, we introduce a tensor completion model targeted for 3D FM imaging. This model not only aligns with the nature of FM imaging, like nonlinearity and incompleteness, but also offers a principled framework for capturing the underlying structural patterns of cell volumes, enabling accurate 3D cell recovery. Furthermore, we derive the lower bound for exact 3D cell completion based on the proposed cell tensor completion model.
- Through solving the proposed cell tensor completion model, we derive a mathematically equivalent score-based diffusion model by reformulating the low-rank tensor recovery as a conditional generative process. This model is further guided by structural consistency priors to steer the generative trajectory toward accurate and denoised 3D FM reconstruction.
- Evaluations on SR-CACO-2 and three real *in vivo* cellular datasets confirm that our method outperforms existing approaches, with clear gains in both SNR and structural fidelity.

2 Problem Formulations

2.1 3D FM Live Cell Imaging

FM imaging is a complex process involving light excitation, fluorescence emission, and diffraction through optical components [22], all of which are nonlinear and influenced by diverse optical and biological interactions [23]. It is further challenged by high noise levels—such as optical noise, background interference, and low SNR—especially under low-light or high-speed conditions [31]. Additionally, due to sample heterogeneity and signal attenuation or scattering, the captured data are often incomplete [32]. An illustration of the FM imaging process is shown in Fig. 1.

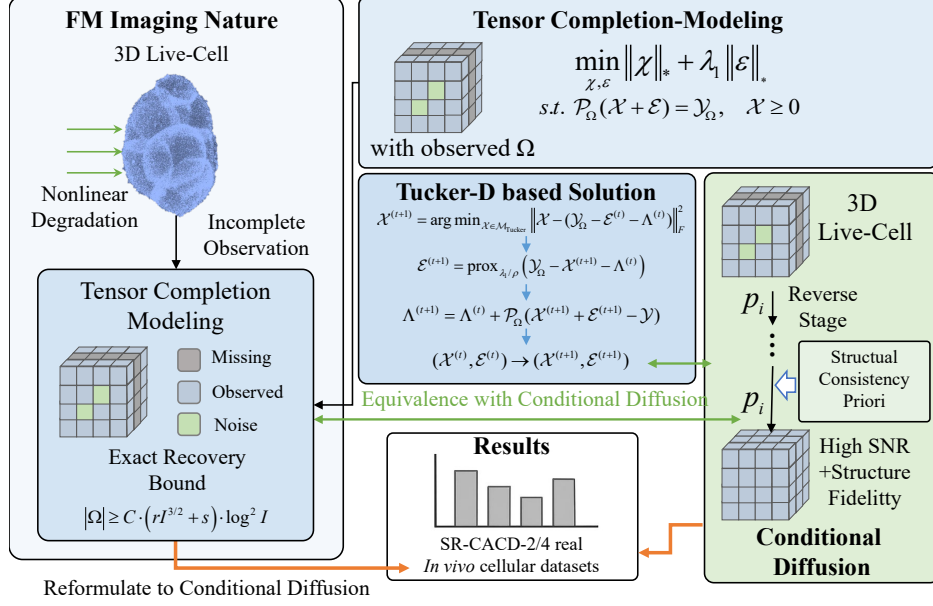


Figure 2: Overview of the proposed framework. We first model 3D fluorescence microscopy (FM) restoration as a tensor completion task, capturing the nonlinear degradation and partial observation inherent in FM imaging. Then, we reformulate this task into a mathematically equivalent score-based generative process, revealing a principled connection to conditional diffusion modeling. Finally, we introduce structural consistency priors to guide the generative trajectory, enabling accurate and denoised 3D cell volume recovery.

Most of image restoration methods based on inverse problem modeling typically assume linearity and well-defined physical models [25], which fail to capture the nonlinearities and sample complexity inherent in FM imaging [27]. Under noisy conditions, these models often become unstable [33], where minor input perturbations lead to large reconstruction errors [30]. Such limitations result in unreliable reconstructions, which are unacceptable in life science applications, as demonstrated in Fig. 1.

$$\hat{I}_y = \mathcal{F}(I_x; \theta), \quad (1)$$

where I_x denotes the low-resolution image, \hat{I}_y is the high-resolution estimate, and $\mathcal{F}(\cdot)$ represents the restoration model, approximating the inverse of the degradation process $\mathcal{D}(\cdot)$. Although \mathcal{D} is typically unknown and influenced by various factors, it is often simplified as a single downsampling operation: $\mathcal{D}(I_y; \delta) = (I_y) \downarrow_s$, where $s \subset \delta$ and \downarrow_s denotes downsampling with scale factor s , typically via bicubic interpolation with antialiasing [7].

Compared to inverse problem-based methods, tensor completion offers key advantages for FM imaging. In 3D FM cell scenarios with the nature of nonlinearity and incompleteness, tensor completion effectively leverages the low-rank structure of multi-dimensional data to recover missing information [34], with inherent robustness to noise [35], where inverse methods often suffer from instability. As a result, tensor completion can yield more consistent and reliable reconstructions—crucial for downstream life science applications. More details of the motivations and advantages are presented in Appendix B.

2.2 Tensor Completion Model for 3D FM Cell Recovery

From the above discussion, the basic tensor completion formulation is shown as follows: Specifically, given a tensor $\mathcal{T} \in \mathbb{R}^{I_1 \times \dots \times I_k}$ with observed entries on index set Ω , the recovery is formulated as the solution to the following convex optimization problem to recover \mathcal{X} that adheres to both structural priors and natural image characteristics:

$$\min_{\mathcal{X}} \|\mathcal{X}\|_* \quad \text{s.t.} \quad \mathcal{P}_{\Omega}(\mathcal{X}) = \mathcal{P}_{\Omega}(\mathcal{T}), \quad (2)$$

As 3D FM cell volumes are typically incomplete due to the nonlinear imaging process, the sampling of cell entries in the tensor completion formulation, $\mathcal{P}_{\Omega}(\mathcal{X})$, with an appropriate sampling distribution, effectively captures the incompleteness introduced by fast volumetric scanning in FM imaging. To address the noise

inherent in the FM imaging process, the tensor completion model should exhibit robustness to noise. Thus, we further optimize the formulation:

$$\begin{aligned} \min_{\mathcal{X}, \mathcal{E}} \quad & \|\mathcal{X}\|_* + \lambda_1 \|\mathcal{E}\|_1 \\ \text{s.t.} \quad & \mathcal{P}_\Omega(\mathcal{X} + \mathcal{E}) = \mathcal{Y}_\Omega, \quad \mathcal{X} \geq 0 \end{aligned} \quad (3)$$

where $\|\mathcal{X}\|_*$ denotes a tensor nuclear norm (e.g., tubal nuclear norm), enforcing low-rank structure, $\|\mathcal{E}\|_1$ penalizes sparse noise or corruption, \mathcal{P}_Ω is the projection operator onto the observed entries.

By modeling 3D cell recovery as a tensor completion problem, it becomes possible to more effectively address both the issue of missing entries and inherent noise in the cell tensor, thereby achieving better alignment with the imaging nature of 3D cellular structures. It is worth noting that this formulation still lacks the capacity to capture the underlying core pattern of the cell volume, which will be introduced in Section 3.1.

2.3 Lower Bound for Exact Cell Recovery

In this subsection, we derive the lower bound for exact cell recovery under the formulation of Eq. 3, based on a sampling distribution Ω that aligns with the characteristics of FM imaging.

First, we present the lower bound for exact cell recovery under the formulation of Eq. 2, and further extend it to the more general formulation given in Eq. 3. The lower bound for exact cell recovery under Eq. 2 is shown as below. To conserve space, the proof is provided in Appendix E.

Theorem 1 (Exact Recovery Lower Bound under Eq. 2) *Let Ω be a uniformly sampled subset of $[I_1] \times \cdots \times [I_k]$ and $\hat{\mathcal{T}}$ be the solution to (1) with $\delta_j = \sqrt{\lambda_* r_* / I_j}$. The reason of the sampling of FM imaging serving as a uniformly sampling is shown in Appendix E. There exists a constant $c_k > 0$ depending on k only so that $\mathbb{P}\{\hat{\mathcal{T}} = \mathcal{T}\} \geq 1 - I^{-\beta}$ if*

$$\lambda_* \geq \frac{1}{r_*} \max_{1 \leq j \leq k} \{\mu_j(\mathcal{T}) r_j(\mathcal{T})\}, \quad (4)$$

and

$$\begin{aligned} n := |\Omega| \geq c_k (1 + \beta) \Big(& (\mu_* + \alpha_*^2 \lambda_*^{k-2}) r_*^{k-1} I (\log I)^2 \\ & + \alpha_* \lambda_*^{k/2-1} r_*^{(k-1)/2} I^{3/2} (\log I)^2 \Big), \end{aligned} \quad (5)$$

where $I = \max_j I_j$, r_* denotes the effective rank of the tensor, and λ_* is normalized rank scaling factor. Thus, the requirements of exact cell tensor recovery under is $\mathcal{O}((rI^{3/2} + r^2 I) \log^2 I)$.

Theorem 2 (Exact Recovery Lower Bound under Eq. 3) *Let $\mathcal{T} = \mathcal{X} + \mathcal{E} \in \mathbb{R}^{I_1 \times \cdots \times I_k}$ be a tensor consisting of a low-rank component \mathcal{X} and a sparse corruption \mathcal{E} , with observed entries given by index set $\Omega \subset [I_1] \times \cdots \times [I_k]$. Suppose the support of \mathcal{E} is uniformly distributed within Ω , and sparsity level is $s = \|\mathcal{E}\|_0$. Then there exists a constant $C > 0$ such that exact recovery $\hat{\mathcal{X}} = \mathcal{X}, \hat{\mathcal{E}} = \mathcal{E}$ holds with high probability provided the number of observed entries satisfies:*

$$|\Omega| \geq C \cdot (rI^{3/2} + s) \cdot \log^2 I, \quad (6)$$

where r denotes the tensor rank and $I = \max\{I_1, \dots, I_k\}$.

In the experiment section, we estimate the rank of the cell tensor and observe that, under the sampling rate of confocal fluorescence microscopy, the number of observed entries in the 3D cell volume exceeds the derived lower bound. This indicates the possibility of exact recovery for 3D cell structures.

3 Proposed Solution

As discussed above, the robust cell tensor completion in Eq. 3 is better suited for handling FM imaging with nonlinearity and incompleteness. In this section, we further provide a principled solution to this optimization problem with capturing the core pattern underlying 3D cell. Then, we derive the equivalence between this solution and a conditional diffusion process, elegantly reformulating low-rank tensor recovery as a conditional generative process. The details of the proposed method can be seen in Fig. 2

3.1 Tucker Decomposition-based Solution

For Eq. 3, the Tucker decomposition is an effective tool as it models the 3D FM cell through a low-rank core tensor and mode-specific factor matrices [36]. This allows it to extract global spatial correlations, reduce redundancy, and isolate the dominant structural components across different dimensions—making it particularly suitable for recovering incomplete and noisy 3D biomedical images. Then, the Tucker decomposition is shown as:

$$\mathcal{X} = \mathcal{G} \times_1 U^{(1)} \times_2 U^{(2)} \times_3 U^{(3)}, \quad (7)$$

where $\mathcal{G} \in \mathbb{R}^{r_1 \times r_2 \times r_3}$ and $U^{(n)} \in \mathbb{R}^{I_n \times r_n}$ are the core tensor and factor matrices, respectively. The reformulated optimization becomes:

$$\min_{\mathcal{G}, \{U^{(n)}\}, \mathcal{E}} \|\mathcal{G}\|_F^2 + \lambda_1 \|\mathcal{E}\|_1 \quad \text{s.t.} \quad \mathcal{P}_\Omega(\mathcal{G} \times_1 U^{(1)} \times_2 U^{(2)} \times_3 U^{(3)} + \mathcal{E}) = \mathcal{Y}_\Omega. \quad (8)$$

We decompose the original problem into subproblems and apply an alternating update scheme over the core tensor, factor matrices, and sparse error. The update steps iteratively refine the recovered tensor, gradually denoising and completing the missing entries. However, due to challenges in modeling noise and handling sparse sampling, a closed-form solution is difficult to obtain under minimal assumptions.

We address this using the strategy detailed in Appendix F, which decomposes the problem into tractable subproblems and solves it via alternating updates. The key processes are summarized as follows:

Step 1: Update the core tensor $\mathcal{G}^{(t+1)}$. Given the factor matrices $\{U^{(n)}\}_{n=1}^3$, the sparse noise estimate $\mathcal{E}^{(t)}$, and the dual variable $\Lambda^{(t)}$, we update the core tensor $\mathcal{G}^{(t+1)}$ by solving a least squares problem:

$$\mathcal{G}^{(t+1)} = \arg \min_{\mathcal{G}} \|\mathcal{G}\|_F^2 + \frac{\rho}{2} \left\| \mathcal{P}_\Omega \left(\mathcal{G} \times_1 U^{(1)} \times_2 U^{(2)} \times_3 U^{(3)} + \mathcal{E}^{(t)} - \mathcal{Y} + \Lambda^{(t)} \right) \right\|_F^2, \quad (9)$$

where $\Lambda^{(t)}$ is the dual variable. Step 2: Update the factor matrix $U^{(n)}$. Fixing the newly updated core tensor $\mathcal{G}^{(t+1)}$, we sequentially update each factor matrix $U^{(n)}$ by minimizing the projection error with respect to observed entries:

$$U^{(n)} = \arg \min_U \left\| \mathcal{P}_\Omega \left(\mathcal{G}^{(t+1)} \times_1 U^{(1)} \cdots \times_n U \cdots \times_3 U^{(3)} + \mathcal{E}^{(t)} - \mathcal{Y} \right) \right\|_F^2, \quad n = 1, 2, 3. \quad (10)$$

Step 3: Update the sparse noise tensor $\mathcal{E}^{(t+1)}$. After reconstructing the current estimate of the clean tensor, we update the sparse noise tensor $\mathcal{E}^{(t+1)}$ via the soft-thresholding operation:

$$\mathcal{E}^{(t+1)} = \text{SoftThreshold}_{\lambda_1/\rho} \left(\mathcal{Y}_\Omega - \mathcal{X}_\Omega^{(t+1)} - \Lambda^{(t)} \right), \quad (11)$$

where soft-thresholding is applied element-wise: $\text{SoftThreshold}_\tau(x) = \text{sign}(x) \cdot \max(|x| - \tau, 0)$. Step 4: Update the dual variable $\Lambda^{(t+1)}$. To enforce the equality constraint in Eq. (3), we update the dual variable using the standard ADMM rule:

$$\Lambda^{(t+1)} = \Lambda^{(t)} + \mathcal{P}_\Omega \left(\mathcal{X}^{(t+1)} + \mathcal{E}^{(t+1)} - \mathcal{Y} \right). \quad (12)$$

Step 5: Reconstruct the low-rank tensor $\mathcal{X}^{(t+1)}$. Finally, we reconstruct the full tensor estimate $\mathcal{X}^{(t+1)}$ using the updated core tensor and factor matrices:

$$\mathcal{X}^{(t+1)} = \mathcal{G}^{(t+1)} \times_1 U^{(1)} \times_2 U^{(2)} \times_3 U^{(3)}. \quad (13)$$

As this optimization lacks a closed-form solution, it relies on iterative refinement. Interestingly, this multi-step update process mirrors the reverse dynamics of diffusion models. Motivated by this connection, we next formulate a conditional diffusion model that incorporates structural consistency priors to guide accurate and denoised 3D FM image reconstruction.

3.2 Equivalence with Conditional Diffusion Framework

Interestingly, the multi-step refinement process above in our optimization closely resembles the reverse trajectory of a diffusion model. Motivated by this observation, we establish a theoretical equivalence between our iterative solution and a conditional diffusion framework. Let the observed 3D FM image tensor be represented as $\mathcal{Y}_\Omega = \mathcal{X}_\Omega + \mathcal{E}_\Omega$, where $\Omega \subset [I_1] \times [I_2] \times [I_3]$ denotes the index set of known entries, and \mathcal{E}_Ω is additive sparse noise. The solution to the robust low-rank tensor recovery problem:

$$\min_{\mathcal{X}, \mathcal{E}} \|\mathcal{X}\|_* + \lambda_1 \|\mathcal{E}\|_1 \quad \text{s.t.} \quad \mathcal{P}_\Omega(\mathcal{X} + \mathcal{E}) = \mathcal{Y}_\Omega, \quad \mathcal{X} \geq 0, \quad (14)$$

where Tucker projection $\mathcal{X}^{(t+1)}$ serves as score-guided denoising, Sparse corruption $\mathcal{E}^{(t)}$ models forward noise, and Observation \mathcal{Y}_Ω provides the conditioning signal. Let $\mathcal{X} = \mathcal{G} \times_1 U^{(1)} \times_2 U^{(2)} \times_3 U^{(3)}$ be the Tucker decomposition of the clean latent tensor. Consider the following iterative updates in ADMM [37]: firstly, Tucker Projection Step (Structure prior inference):

$$\mathcal{X}^{(t+1)} = \arg \min_{\mathcal{X} \in \mathcal{M}_{\text{Tucker}}} \left\| \mathcal{X} - (\mathcal{Y}_\Omega - \mathcal{E}^{(t)} - \Lambda^{(t)}) \right\|_F^2, \quad (15)$$

where $\mathcal{M}_{\text{Tucker}}$ denotes the low-rank Tucker manifold. This is equivalent to a MAP inference step under a Gaussian prior over \mathcal{X} , constrained by the current denoised observation [38]. In the language of diffusion models, this mimics the learned score-function $\nabla \log p_\theta(\mathcal{X}^{(t)} | \mathcal{Y}_\Omega)$ [39]. Then, Sparse Noise Estimation (Forward process inversion):

$$\mathcal{E}^{(t+1)} = \text{prox}_{\lambda_1/\rho} \left(\mathcal{Y}_\Omega - \mathcal{X}^{(t+1)} - \Lambda^{(t)} \right), \quad (16)$$

which corresponds to soft-thresholding the residual, and is equivalent to denoising Gaussian-like noise in DDPM [40]. finally, Dual Variable Update (Lagrangian residual accumulation):

$$\Lambda^{(t+1)} = \Lambda^{(t)} + \mathcal{P}_\Omega(\mathcal{X}^{(t+1)} + \mathcal{E}^{(t+1)} - \mathcal{Y}). \quad (17)$$

Together, these three steps define a deterministic Markov transition:

$$(\mathcal{X}^{(t)}, \mathcal{E}^{(t)}) \rightarrow (\mathcal{X}^{(t+1)}, \mathcal{E}^{(t+1)}), \quad (18)$$

which approximates the reverse sampling trajectory:

$$x_{t-1} = \mu_\theta(x_t, c) + \Sigma_t^{1/2} z, \quad (19)$$

in the diffusion process conditioned on input $c = \mathcal{Y}_\Omega$, with the difference that our method achieves this without learning the score model, instead using manifold projections and proximal operators.

When solved via an ADMM framework using Tucker decomposition of \mathcal{X} , yields an iterative sequence $\{\mathcal{X}^{(t)}\}$ that is mathematically equivalent to a discrete-time conditional diffusion reverse process, i.e., the Tucker-based iterative recovery process constitutes a deterministic, optimization-driven analog of the conditional diffusion reverse chain:

$$x_{t-1} = \frac{1}{\sqrt{\alpha_t}} \left(x_t - \frac{1 - \alpha_t}{\sqrt{1 - \bar{\alpha}_t}} \epsilon_\theta(x_t, c) \right) + \sigma_t z, \quad (20)$$

where $\alpha_t = 1 - \beta_t$, and β_t is the noise variance added at step t ; $\bar{\alpha}_t$ is defined as the cumulative product: $\bar{\alpha}_t = \prod_{s=1}^t \alpha_s$; σ_t is the variance of the Gaussian noise added back in the reverse process. This equivalence not only provides theoretical insight into the optimization procedure but also motivates a principled generative framework for 3D FM cell reconstruction. In the supplementary materials, we present the details of the conditional diffusion model with structural consistency priors.

4 Experiments

We evaluate our method on three 3D fluorescence microscopy datasets, including SR-CACO-2 [41] and other *in vivo* cellular volumes. We focus on two tasks: 3D super-resolution from sparse Z-axis sampling and denoising under low SNR conditions. The datasets and the settings are introduced in details in Appendix G. Due to space limitations, a more detailed analysis is provided in Appendix A.

4.1 Main Results

We compare our method with state-of-the-art baselines on SR-CACO-2 and two *in vivo* datasets using multiple metrics. The benchmarks include FM-specific and general restoration methods. We also provide visual results and analyze temporal consistency and performance distributions across datasets.

4.1.1 Quantitative Comparison with State-of-the-Art Methods

Table 1 compares our method with baseline models on SR-CACO-2 and two *in vivo* cellular datasets. On all three dataset, our method achieves the best overall performance, with the highest PSNR, SSIM, and NRQM, indicating superior fidelity and perceptual quality. Compared to DDPM, we show clear improvements in

Table 1: Performance comparison of our method and other methods under SR-CACO-2 and two datasets of *in vivo* cellular volumes.

Model	PSNR \uparrow	SSIM \uparrow	LPIPS \downarrow	NIQE \downarrow	PIQE \downarrow	NRQM \uparrow
<i>C. elegans</i> evaluation dataset 1						
DBPN	31.89	0.6122	<i>0.3941</i>	19.05	<i>44.43</i>	4.23
Neuroclear	30.56	0.5798	0.6122	20.87	40.17	2.49
Cycle+HAT	<i>32.37</i>	0.6236	0.4069	<i>18.95</i>	42.98	4.38
Cycle+IPG	32.17	<i>0.6338</i>	0.4640	19.97	41.50	4.36
DDPM (Baseline)	31.49	0.6157	0.4221	19.06	41.01	4.65
Ours	33.18	0.6682	0.3773	17.89	46.27	4.51
<i>C. elegans</i> evaluation dataset 2						
DBPN	37.91	0.9631	0.3872	19.11	46.11	3.95
Neuroclear	36.75	0.8405	0.5654	19.51	53.00	3.59
Cycle+HAT	<i>39.86</i>	0.9726	0.3648	20.53	48.64	4.51
Cycle+IPG	37.92	0.9519	<i>0.3138</i>	19.37	46.46	<i>4.69</i>
DDPM(Baseline)	36.96	<i>0.9766</i>	0.3708	<i>18.93</i>	<i>44.78</i>	4.59
Ours	40.95	0.9868	0.2674	18.74	44.28	4.83
<i>SR-CACO-2</i>						
DBPN	37.34	0.7871	0.5071	10.13	69.23	1.34
Neuroclear	33.93	0.7236	0.6182	11.78	88.30	2.74
Cycle+HAT	39.35	0.9313	<i>0.3036</i>	8.56	65.71	3.70
Cycle+IPG	39.82	0.9428	0.3369	8.85	<i>66.27</i>	3.87
DDPM(Baseline)	<i>40.24</i>	<i>0.9447</i>	0.3679	8.83	78.98	<i>3.97</i>
Ours	40.30	0.9476	0.2305	<i>8.66</i>	70.27	4.09

LPIPS and NRQM while maintaining comparable distortion-based metrics. Specifically, on *C. elegans* dataset 1, our method achieves the best PSNR/SSIM and strong LPIPS, offering a good balance between perceptual quality and structural accuracy. In *C. elegans* dataset 2, our method again achieves the top PSNR and SSIM, and outperforms all baselines in LPIPS, NIQE, and PIQE, confirming its robustness under real biological conditions.

Overall, the results highlight the strong generalization and reconstruction capabilities of our diffusion-guided framework across both synthetic and real-world microscopy data.

4.1.2 Qualitative Comparison with State-of-the-Art Methods

3D/Slice/Zoom-in Visual Comparison. To evaluate structural fidelity and robustness, we compare reconstruction results at two representative time points (Fig. 3). Under low-SNR conditions, raw inputs show heavy noise and blurred membranes. Bicubic fails to restore details, while DBPN introduces over-smoothing. Unsupervised methods like Cycle+IPG and Cycle+HAT often distort structures. Although Neuroclear improves sharpness, it lacks consistency. In contrast, our method reliably recovers continuous and biologically plausible membranes, preserving fine details and suppressing noise. These results highlight the temporal generalization and structural accuracy of our diffusion-guided reconstruction.

Performance Statistics Analysis. We assess reconstruction quality on SR-CACO-2 and three *C. elegans* datasets using PSNR and LPIPS. As shown in Fig. 8 (a), our method yields high and stable PSNR, especially on SR-CACO-2. Fig. 8 (b) shows consistently low LPIPS across XY and YZ planes, indicating strong perceptual quality. SR-CACO-2 achieves the lowest LPIPS, while *C. elegans* scores remain slightly higher due to structural complexity. The consistent performance across planes highlights our method’s robustness on anisotropic data and real biological volumes.

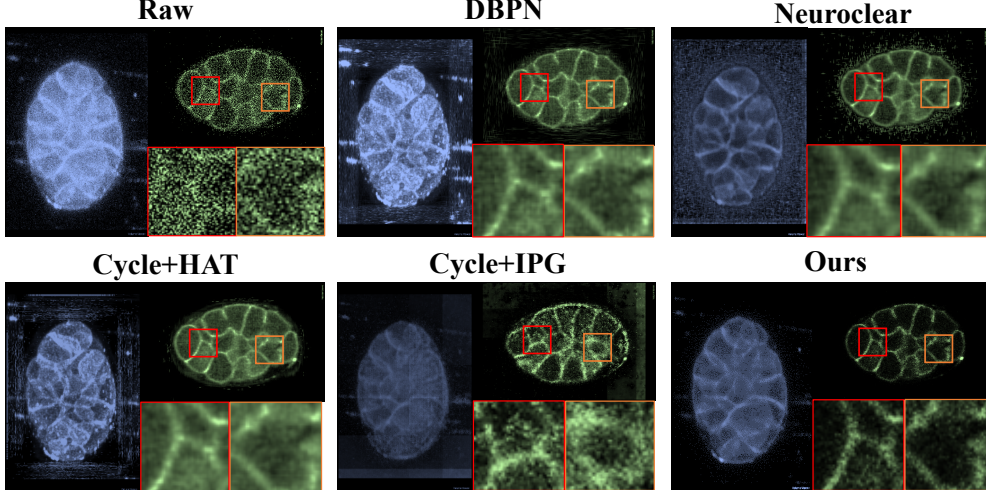


Figure 3: 3D/XY-Slice/Zoom-in qualitative denoising comparison of different methods on live 3D fluorescence microscopy volumes at the 2700s time point. Appendix A show the performance comparison at the 4950s time point.

Temporal Robustness Analysis. We also evaluate the temporal robustness of our method on a sequence of *in vivo* FM images from 2700s to 5400s. Due to low-SNR conditions, raw observations show severe noise and structural degradation. As shown in Fig. 9, our method consistently enhances structural fidelity and suppresses noise over time, demonstrating stable and reliable performance across extended temporal sequences.

4.2 Discussion

In this section, we further validate the effectiveness and rationality of our model and methods from multiple perspectives. First, we analyze the distribution of cell volume ranks in the SR-CACO-2 dataset, showing that the number of observed entries slightly exceeds the theoretical recovery bound we derived. Then, we evaluate the performance of our method under varying downsampling rates and noise levels, demonstrating its robustness to noise. As the downsampling rate increases, the number of observations falls below the exact recovery threshold, leading to a noticeable drop in performance.

4.2.1 Rank Distribution of FM Cell

Figure 7 shows that cell volumes exhibit a bimodal rank distribution, with dominant modes around 15 and 30. The average rank is 20.83, indicating varying structural complexity across samples. This highlights the need for adaptive low-rank modeling. Figure 7 displays the distribution of the lower observed bound for exact recovery. Most samples lie well above the theoretical bound for rank 10, suggesting sufficient observations for recovery in practice. However, the multimodal pattern implies that some samples may still challenge fixed recovery thresholds.

4.2.2 Performance Under Different Sampling Densities and Noise

As shown in Table 2, our method maintains stable performance under increasing noise and downsampling. PSNR and SSIM gradually decrease with higher noise levels and downsampling factors, while LPIPS, NIQE, and PIQE increase as expected. Despite these degradations, the quality drops remain smooth and moderate, demonstrating the robustness of our approach in handling low-SNR and low-resolution conditions.

5 Conclusion

We propose a structure-aware unsupervised method for 3D FM reconstruction, which reformulates tensor completion as a conditional diffusion process. It improves denoising and axial resolution while preserving fine cellular structures, demonstrating strong performance across diverse *in vivo* datasets. Our method provides

Table 2: Performance comparison under *in vivo* cellular dataset with various noise levels and downsampling factors (*C. elegans* evaluation dataset 1).

Setting	PSNR \uparrow	SSIM \uparrow	LPIPS \downarrow	NIQE \downarrow	PIQE \downarrow	NRQM \uparrow
Original (Clean)	33.18	0.6682	0.3773	17.89	46.27	4.51
+ Gaussian noise ($\sigma = 0.01$)	32.58	0.6427	0.3953	18.44	50.42	4.34
+ Gaussian noise ($\sigma = 0.05$)	31.26	0.6257	0.4253	19.86	57.58	4.01
+ Gaussian noise ($\sigma = 0.1$)	29.34	0.5921	0.4606	21.22	65.05	3.65
+ Downsampling $\times 2$	31.53	0.6354	0.4051	18.87	52.57	4.28
+ Downsampling $\times 3$	29.67	0.6102	0.4443	19.92	58.33	3.91
+ Downsampling $\times 4$	29.01	0.5955	0.4755	21.07	63.51	3.69

clearer observations, helping to reveal biological patterns and support discoveries in developmental biology and disease understanding.

References

- [1] AR Sheldrake. The ageing, growth and death of cells. *Nature*, 250(5465):381–385, 1974.
- [2] Cara M Winter, Pablo Szekely, Vladimir Popov, Heather Belcher, Raina Carter, Matthew Jones, Scott E Fraser, Thai V Truong, and Philip N Benfey. Shr and scr coordinate root patterning and growth early in the cell cycle. *Nature*, 626(7999):611–616, 2024.
- [3] Zelin Li, Chenwei Wang, Zhaoke Huang, Yiming Ma, Cunming Zhao, Zhongying Zhao, and Hong Yan. Volume tells: Dual cycle-consistent diffusion for 3d fluorescence microscopy de-noising and super-resolution. In *Proceedings of the Computer Vision and Pattern Recognition Conference*, pages 16091–16100, 2025.
- [4] Kwanghun Chung, Jenelle Wallace, Sung-Yon Kim, Sandhiya Kalyanasundaram, Aaron S Andelman, Thomas J Davidson, Julie J Mirzabekov, Kelly A Zalocusky, Joanna Mattis, Aleksandra K Denisin, et al. Structural and molecular interrogation of intact biological systems. *Nature*, 497(7449):332–337, 2013.
- [5] Venkatakaushik Voleti, Kripa B Patel, Wenze Li, Citlali Perez Campos, Srinidhi Bharadwaj, Hang Yu, Caitlin Ford, Malte J Casper, Richard Wenwei Yan, Wenxuan Liang, et al. Real-time volumetric microscopy of *in vivo* dynamics and large-scale samples with scape 2.0. *Nature methods*, 16(10):1054–1062, 2019.
- [6] Chenwei Wang, Renjie Xu, Yulin Huang, Jifang Pei, Chuan Huang, Wenqi Zhu, and Jianyu Yang. Limited-data sar atr causal method via dual-invariance intervention. *IEEE Transactions on Geoscience and Remote Sensing*, 2025.
- [7] Chenwei Wang, Jifang Pei, Zhiyong Wang, Yulin Huang, Junjie Wu, Haiguang Yang, and Jianyu Yang. When deep learning meets multi-task learning in sar atr: Simultaneous target recognition and segmentation. *Remote Sensing*, 12(23):3863, 2020.
- [8] Chao Dong, Chen Change Loy, Kaiming He, and Xiaoou Tang. Image super-resolution using deep convolutional networks. *IEEE Transactions on Pattern Analysis and Machine Intelligence*, 38(2):295–307, 2016.
- [9] Chao Dong, Chen Change Loy, and Xiaoou Tang. Accelerating the super-resolution convolutional neural network. In Bastian Leibe, Jiri Matas, Nicu Sebe, and Max Welling, editors, *Computer Vision – ECCV 2016*, pages 391–407, Cham, 2016. Springer International Publishing.
- [10] Chenwei Wang, Siyi Luo, Jifang Pei, Xiaoyu Liu, Yulin Huang, Yin Zhang, and Jianyu Yang. An entropy-awareness meta-learning method for sar open-set atr. *IEEE Geoscience and Remote Sensing Letters*, 2023.
- [11] Jonathan Ho, Ajay Jain, and Pieter Abbeel. Denoising diffusion probabilistic models. In H. Larochelle, M. Ranzato, R. Hadsell, M.F. Balcan, and H. Lin, editors, *Advances in Neural Information Processing Systems*, volume 33, pages 6840–6851. Curran Associates, Inc., 2020.
- [12] Jun-Yan Zhu, Taesung Park, Phillip Isola, and Alexei A. Efros. Unpaired image-to-image translation using cycle-consistent adversarial networks. In *Proceedings of the IEEE International Conference on Computer Vision (ICCV)*, Oct 2017.

- [13] Yuan Yuan, Siyuan Liu, Jiawei Zhang, Yongbing Zhang, Chao Dong, and Liang Lin. Unsupervised image super-resolution using cycle-in-cycle generative adversarial networks. In *Proceedings of the IEEE Conference on Computer Vision and Pattern Recognition (CVPR) Workshops*, June 2018.
- [14] Dmitry Ulyanov, Andrea Vedaldi, and Victor Lempitsky. Deep image prior. In *Proceedings of the IEEE Conference on Computer Vision and Pattern Recognition (CVPR)*, June 2018.
- [15] Kefu Ning, Bolin Lu, Xiaojun Wang, Xiaoyu Zhang, Shuo Nie, Tao Jiang, Anan Li, Guoqing Fan, Xiaofeng Wang, Qingming Luo, Hui Gong, and Jing Yuan. Deep self-learning enables fast, high-fidelity isotropic resolution restoration for volumetric fluorescence microscopy. *Light: Science & Applications*, 12(1):204, Aug 2023.
- [16] Liying Qu, Shiqun Zhao, Yuanyuan Huang, Xianxin Ye, Kunhao Wang, Yuzhen Liu, Xianming Liu, Heng Mao, Guangwei Hu, Wei Chen, Changliang Guo, Jiaye He, Jiubin Tan, Haoyu Li, Liangyi Chen, and Weisong Zhao. Self-inspired learning for denoising live-cell super-resolution microscopy. *Nature Methods*, 21(10):1895–1908, Oct 2024.
- [17] Hyoungjun Park, Myeongsu Na, Bumju Kim, Soohyun Park, Ki Hean Kim, Sunghoe Chang, and Jong Chul Ye. Deep learning enables reference-free isotropic super-resolution for volumetric fluorescence microscopy. *Nature Communications*, 13(1):3297, Jun 2022.
- [18] Xinyang Li, Xiaowan Hu, Xingye Chen, Jiaqi Fan, Zhifeng Zhao, Jiamin Wu, Haoqian Wang, and Qionghai Dai. Spatial redundancy transformer for self-supervised fluorescence image denoising. *Nature Computational Science*, 3(12):1067–1080, Dec 2023.
- [19] Qinghua Wang, Ziwei Li, Shuqi Zhang, Nan Chi, and Qionghai Dai. A versatile wavelet-enhanced cnn-transformer for improved fluorescence microscopy image restoration. *Neural Networks*, 170:227–241, 2024.
- [20] Chenwei Wang, Siyi Luo, Yulin Huang, Jifang Pei, Yin Zhang, and Jianyu Yang. Sar atr method with limited training data via an embedded feature augmenter and dynamic hierarchical-feature refiner. *IEEE Transactions on Geoscience and Remote Sensing*, 2023.
- [21] Chenwei Wang, Yulin Huang, Xiaoyu Liu, Jifang Pei, Yin Zhang, and Jianyu Yang. Global in local: A convolutional transformer for sar atr fsl. *IEEE Geoscience and Remote Sensing Letters*, 19:1–5, 2022.
- [22] Jeff W Lichtman and José-Angel Conchello. Fluorescence microscopy. *Nature methods*, 2(12):910–919, 2005.
- [23] Chris Xu, Maiken Nedergaard, Deborah J Fowell, Peter Friedl, and Na Ji. Multiphoton fluorescence microscopy for in vivo imaging. *Cell*, 187(17):4458–4487, 2024.
- [24] Chenwei Wang, Xiaoyu Liu, Yulin Huang, Siyi Luo, Jifang Pei, Jianyu Yang, and Deqing Mao. Semi-supervised sar atr framework with transductive auxiliary segmentation. *Remote Sensing*, 14(18):4547, 2022.
- [25] Jérôme Sol, Hugo Prod'homme, Luc Le Magoarou, and Philipp Del Hougne. Experimentally realized physical-model-based frugal wave control in metasurface-programmable complex media. *Nature Communications*, 15(1):2841, 2024.
- [26] Yanquan Mo, Kunhao Wang, Liuju Li, Shijia Xing, Shouhua Ye, Jiayuan Wen, Xinxin Duan, Ziying Luo, Wen Gou, Tongsheng Chen, et al. Quantitative structured illumination microscopy via a physical model-based background filtering algorithm reveals actin dynamics. *Nature communications*, 14(1):3089, 2023.
- [27] Mude Hui, Zihao Wei, Hongru Zhu, Fei Xia, and Yuyin Zhou. Microdiffusion: Implicit representation-guided diffusion for 3d reconstruction from limited 2d microscopy projections. In *Proceedings of the IEEE/CVF Conference on Computer Vision and Pattern Recognition*, pages 11460–11469, 2024.
- [28] Chenwei Wang, Jifang Pei, Xiaoyu Liu, Yulin Huang, Deqing Mao, Yin Zhang, and Jianyu Yang. Sar target image generation method using azimuth-controllable generative adversarial network. *IEEE Journal of Selected Topics in Applied Earth Observations and Remote Sensing*, 15:9381–9397, 2022.
- [29] Ji Yu and Ahmed Elmokadem. Single-molecule localization microscopy as nonlinear inverse problem. *Proceedings of the National Academy of Sciences*, 116(41):20438–20445, 2019.
- [30] Martin Genzel, Jan Macdonald, and Maximilian März. Solving inverse problems with deep neural networks—robustness included? *IEEE transactions on pattern analysis and machine intelligence*, 45(1):1119–1134, 2022.

- [31] Xinyang Li, Yixin Li, Yiliang Zhou, Jiamin Wu, Zhifeng Zhao, Jiaqi Fan, Fei Deng, Zhaofa Wu, Guihua Xiao, Jing He, et al. Real-time denoising enables high-sensitivity fluorescence time-lapse imaging beyond the shot-noise limit. *Nature Biotechnology*, 41(2):282–292, 2023.
- [32] Henry Pinkard, Hratch Baghdassarian, Adriana Mujal, Ed Roberts, Kenneth H Hu, Daniel Haim Friedman, Ivana Malenica, Taylor Shagam, Adam Fries, Kaitlin Corbin, et al. Learned adaptive multiphoton illumination microscopy for large-scale immune response imaging. *Nature communications*, 12(1):1916, 2021.
- [33] Vegard Antun, Francesco Renna, Clarice Poon, Ben Adcock, and Anders C Hansen. On instabilities of deep learning in image reconstruction and the potential costs of ai. *Proceedings of the National Academy of Sciences*, 117(48):30088–30095, 2020.
- [34] Donald Goldfarb and Zhiwei Qin. Robust low-rank tensor recovery: Models and algorithms. *SIAM Journal on Matrix Analysis and Applications*, 35(1):225–253, 2014.
- [35] Hao Wang, Jiaxin Yang, Xinrui Yu, Yu Zhang, Jianliang Qian, and Jianrong Wang. Tensor-flamingo unravels the complexity of single-cell spatial architectures of genomes at high-resolution. *Nature Communications*, 16(1):3435, 2025.
- [36] Tamara G Kolda and Brett W Bader. Tensor decompositions and applications. *SIAM review*, 51(3):455–500, 2009.
- [37] Minru Bai, Xiongjun Zhang, Guyan Ni, and Chunfeng Cui. An adaptive correction approach for tensor completion. *SIAM Journal on Imaging Sciences*, 9(3):1298–1323, 2016.
- [38] Daniel Kressner, Michael Steinlechner, and Bart Vandereycken. Low-rank tensor completion by riemannian optimization. *BIT Numerical Mathematics*, 54:447–468, 2014.
- [39] Jascha Sohl-Dickstein, Eric Weiss, Niru Maheswaranathan, and Surya Ganguli. Deep unsupervised learning using nonequilibrium thermodynamics. In *International conference on machine learning*, pages 2256–2265. pmlr, 2015.
- [40] Jonathan Ho, Ajay Jain, and Pieter Abbeel. Denoising diffusion probabilistic models. *Advances in neural information processing systems*, 33:6840–6851, 2020.
- [41] Soufiane Belharbi, Mara Whitford, Phuong Hoang, Shakeeb Murtaza, Luke McCaffrey, and Eric Granger. Sr-caco-2: A dataset for confocal fluorescence microscopy image super-resolution. *Advances in Neural Information Processing Systems*, 37:59948–59983, 2024.
- [42] Chao Dong, Chen Change Loy, Kaiming He, and Xiaoou Tang. Image super-resolution using deep convolutional networks. *IEEE transactions on pattern analysis and machine intelligence*, 38(2):295–307, 2015.
- [43] Jiwon Kim, Jung Kwon Lee, and Kyoung Mu Lee. Accurate image super-resolution using very deep convolutional networks. In *Proceedings of the IEEE conference on computer vision and pattern recognition*, pages 1646–1654, 2016.
- [44] Ying Tai, Jian Yang, and Xiaoming Liu. Image super-resolution via deep recursive residual network. In *Proceedings of the IEEE conference on computer vision and pattern recognition*, pages 3147–3155, 2017.
- [45] Ying Tai, Jian Yang, Xiaoming Liu, and Chunyan Xu. Memnet: A persistent memory network for image restoration. In *Proceedings of the IEEE international conference on computer vision*, pages 4539–4547, 2017.
- [46] Yiqun Mei, Yuchen Fan, and Yuqian Zhou. Image super-resolution with non-local sparse attention. In *Proceedings of the IEEE/CVF conference on computer vision and pattern recognition*, pages 3517–3526, 2021.
- [47] Chang Qiao, Di Li, Yuting Guo, Chong Liu, Tao Jiang, Qionghai Dai, and Dong Li. Evaluation and development of deep neural networks for image super-resolution in optical microscopy. *Nature methods*, 18(2):194–202, 2021.
- [48] Jingyun Liang, Jiezhang Cao, Guolei Sun, Kai Zhang, Luc Van Gool, and Radu Timofte. Swinir: Image restoration using swin transformer. In *Proceedings of the IEEE/CVF international conference on computer vision*, pages 1833–1844, 2021.
- [49] Bee Lim, Sanghyun Son, Heewon Kim, Seungjun Nah, and Kyoung Mu Lee. Enhanced deep residual networks for single image super-resolution. In *Proceedings of the IEEE conference on computer vision and pattern recognition workshops*, pages 136–144, 2017.

- [50] Bin Xia, Yucheng Hang, Yapeng Tian, Wenming Yang, Qingmin Liao, and Jie Zhou. Efficient non-local contrastive attention for image super-resolution. In *Proceedings of the AAAI conference on artificial intelligence*, volume 36, pages 2759–2767, 2022.
- [51] Yawei Li, Yuchen Fan, Xiaoyu Xiang, Denis Demandolx, Rakesh Ranjan, Radu Timofte, and Luc Van Gool. Efficient and explicit modelling of image hierarchies for image restoration. In *Proceedings of the IEEE/CVF Conference on Computer Vision and Pattern Recognition*, pages 18278–18289, 2023.
- [52] Fei Kong, Jinhao Duan, Lichao Sun, Hao Cheng, Renjing Xu, Hengtao Shen, Xiaofeng Zhu, Xiaoshuang Shi, and Kaidi Xu. Act-diffusion: efficient adversarial consistency training for one-step diffusion models. In *Proceedings of the IEEE/CVF Conference on Computer Vision and Pattern Recognition*, pages 8890–8899, 2024.
- [53] Hang Wang, Xuanhong Chen, Bingbing Ni, Yutian Liu, and Jinfan Liu. Omni aggregation networks for lightweight image super-resolution. In *Proceedings of the IEEE/CVF Conference on Computer Vision and Pattern Recognition*, pages 22378–22387, 2023.
- [54] Muhammad Haris, Gregory Shakhnarovich, and Norimichi Ukita. Deep back-projection networks for super-resolution. In *Proceedings of the IEEE conference on computer vision and pattern recognition*, pages 1664–1673, 2018.
- [55] Zhen Li, Jinglei Yang, Zheng Liu, Xiaomin Yang, Gwanggil Jeon, and Wei Wu. Feedback network for image super-resolution. In *Proceedings of the IEEE/CVF conference on computer vision and pattern recognition*, pages 3867–3876, 2019.
- [56] Yifan Wang, Federico Perazzi, Brian McWilliams, Alexander Sorkine-Hornung, Olga Sorkine-Hornung, and Christopher Schroers. A fully progressive approach to single-image super-resolution. In *Proceedings of the IEEE conference on computer vision and pattern recognition workshops*, pages 864–873, 2018.
- [57] Wei-Sheng Lai, Jia-Bin Huang, Narendra Ahuja, and Ming-Hsuan Yang. Fast and accurate image super-resolution with deep laplacian pyramid networks. *IEEE transactions on pattern analysis and machine intelligence*, 41(11):2599–2613, 2018.
- [58] Thomas A Klar, Stefan Jakobs, Marcus Dyba, Alexander Egner, and Stefan W Hell. Fluorescence microscopy with diffraction resolution barrier broken by stimulated emission. *Proceedings of the National Academy of Sciences*, 97(15):8206–8210, 2000.
- [59] Biagio Mandracchia, Xuanwen Hua, Changliang Guo, Jeonghwan Son, Tara Urner, and Shu Jia. Fast and accurate scmos noise correction for fluorescence microscopy. *Nature communications*, 11(1):94, 2020.
- [60] Jiwon Kim, Jung Kwon Lee, and Kyoung Mu Lee. Accurate image super-resolution using very deep convolutional networks. In *Proceedings of the IEEE Conference on Computer Vision and Pattern Recognition (CVPR)*, June 2016.
- [61] Chenwei Wang, Xiaoyu Liu, Jifang Pei, Yulin Huang, Yin Zhang, and Jianyu Yang. Multiview attention cnn-lstm network for sar automatic target recognition. *IEEE Journal of Selected Topics in Applied Earth Observations and Remote Sensing*, 14:12504–12513, 2021.
- [62] Bee Lim, Sanghyun Son, Heewon Kim, Seungjun Nah, and Kyoung Mu Lee. Enhanced deep residual networks for single image super-resolution. In *Proceedings of the IEEE Conference on Computer Vision and Pattern Recognition (CVPR) Workshops*, July 2017.
- [63] Chenwei Wang, Jifang Pei, Minghui Li, Yongchao Zhang, Yulin Huang, and Jianyu Yang. Parking information perception based on automotive millimeter wave sar. In *2019 IEEE Radar Conference (RadarConf)*, pages 1–6. IEEE, 2019.
- [64] Chenwei Wang, Jifang Pei, Xiaoyu Liu, Yulin Huang, and Jianyu Yang. A deep deformable residual learning network for sar image segmentation. In *2021 IEEE Radar Conference (RadarConf21)*, pages 1–5. IEEE, 2021.
- [65] Yulun Zhang, Kunpeng Li, Kai Li, Lichen Wang, Bineng Zhong, and Yun Fu. Image super-resolution using very deep residual channel attention networks. In *Proceedings of the European Conference on Computer Vision (ECCV)*, September 2018.
- [66] Tao Dai, Jianrui Cai, Yongbing Zhang, Shu-Tao Xia, and Lei Zhang. Second-order attention network for single image super-resolution. In *2019 IEEE/CVF Conference on Computer Vision and Pattern Recognition (CVPR)*, pages 11057–11066, 2019.

- [67] Chenwei Wang, Jifang Pei, Zhiyong Wang, Yuling Huang, and Jianyu Yang. Multi-view cnn-lstm neural network for sar automatic target recognition. In *IGARSS 2020-2020 IEEE International Geoscience and Remote Sensing Symposium*, pages 1755–1758. IEEE, 2020.
- [68] Christian Ledig, Lucas Theis, Ferenc Huszar, Jose Caballero, Andrew Cunningham, Alejandro Acosta, Andrew Aitken, Alykhan Tejani, Johannes Totz, Zehan Wang, and Wenzhe Shi. Photo-realistic single image super-resolution using a generative adversarial network. In *Proceedings of the IEEE Conference on Computer Vision and Pattern Recognition (CVPR)*, July 2017.
- [69] Xintao Wang, Ke Yu, Shixiang Wu, Jinjin Gu, Yihao Liu, Chao Dong, Yu Qiao, and Chen Change Loy. Esrgan: Enhanced super-resolution generative adversarial networks. In *Proceedings of the European Conference on Computer Vision (ECCV) Workshops*, September 2018.
- [70] Xintao Wang, Liangbin Xie, Chao Dong, and Ying Shan. Real-esrgan: Training real-world blind super-resolution with pure synthetic data. In *Proceedings of the IEEE/CVF International Conference on Computer Vision (ICCV) Workshops*, pages 1905–1914, October 2021.
- [71] Chenwei Wang, Siyi Luo, Jifang Pei, Yulin Huang, Yin Zhang, and Jianyu Yang. Crucial feature capture and discrimination for limited training data sar atr. *ISPRS Journal of Photogrammetry and Remote Sensing*, 204:291–305, 2023.
- [72] Hanting Chen, Yunhe Wang, Tianyu Guo, Chang Xu, Yiping Deng, Zhenhua Liu, Siwei Ma, Chunjing Xu, Chao Xu, and Wen Gao. Pre-trained image processing transformer. In *Proceedings of the IEEE/CVF Conference on Computer Vision and Pattern Recognition (CVPR)*, pages 12299–12310, June 2021.
- [73] Xiangyu Chen, Xintao Wang, Jiantao Zhou, Yu Qiao, and Chao Dong. Activating more pixels in image super-resolution transformer. In *Proceedings of the IEEE/CVF Conference on Computer Vision and Pattern Recognition (CVPR)*, pages 22367–22377, June 2023.
- [74] Zheng Chen, Yulun Zhang, Jinjin Gu, yongbing zhang, Linghe Kong, and Xin Yuan. Cross aggregation transformer for image restoration. In S. Koyejo, S. Mohamed, A. Agarwal, D. Belgrave, K. Cho, and A. Oh, editors, *Advances in Neural Information Processing Systems*, volume 35, pages 25478–25490. Curran Associates, Inc., 2022.
- [75] Haram Choi, Jeongmin Lee, and Jihoon Yang. N-gram in swin transformers for efficient lightweight image super-resolution. In *Proceedings of the IEEE/CVF Conference on Computer Vision and Pattern Recognition (CVPR)*, pages 2071–2081, June 2023.
- [76] Jingyun Liang, Jiezheng Cao, Guolei Sun, Kai Zhang, Luc Van Gool, and Radu Timofte. Swinir: Image restoration using swin transformer. In *Proceedings of the IEEE/CVF International Conference on Computer Vision (ICCV) Workshops*, pages 1833–1844, October 2021.
- [77] Yupeng Zhou, Zhen Li, Chun-Le Guo, Song Bai, Ming-Ming Cheng, and Qibin Hou. Srformer: Permuted self-attention for single image super-resolution. In *Proceedings of the IEEE/CVF International Conference on Computer Vision (ICCV)*, pages 12780–12791, October 2023.
- [78] Chenwei Wang, Jifang Pei, Siyi Luo, Weibo Huo, Yulin Huang, Yin Zhang, and Jianyu Yang. Sar ship target recognition via multiscale feature attention and adaptive-weighed classifier. *IEEE Geoscience and Remote Sensing Letters*, 20:1–5, 2023.
- [79] Chenwei Wang, Jifang Pei, Jianyu Yang, Xiaoyu Liu, Yulin Huang, and Deqing Mao. Recognition in label and discrimination in feature: A hierarchically designed lightweight method for limited data in sar atr. *IEEE Transactions on Geoscience and Remote Sensing*, 60:1–13, 2022.
- [80] Ze Liu, Yutong Lin, Yue Cao, Han Hu, Yixuan Wei, Zheng Zhang, Stephen Lin, and Baining Guo. Swin transformer: Hierarchical vision transformer using shifted windows. In *Proceedings of the IEEE/CVF International Conference on Computer Vision (ICCV)*, pages 10012–10022, October 2021.
- [81] Yun-Ke Luo, Si-Xin Chen, Lu Zhou, and Yi-Qing Ni. Evaluating railway noise sources using distributed microphone array and graph neural networks. *Transportation Research Part D: Transport and Environment*, 107:103315, 2022.
- [82] Yuanzhe Shang, Wei Pu, Congwen Wu, Danling Liao, Xiaowo Xu, Chenwei Wang, Yulin Huang, Yin Zhang, Junjie Wu, Jianyu Yang, et al. Hdss-net: A novel hierarchically designed network with spherical space classifier for ship recognition in sar images. *IEEE Transactions on Geoscience and Remote Sensing*, 61:1–20, 2023.
- [83] Yuchuan Tian, Hanting Chen, Chao Xu, and Yunhe Wang. Image processing gnn: Breaking rigidity in super-resolution. In *Proceedings of the IEEE/CVF Conference on Computer Vision and Pattern Recognition (CVPR)*, pages 24108–24117, June 2024.

- [84] Qingping Zheng, Ling Zheng, Yuanfan Guo, Ying Li, Songcen Xu, Jiankang Deng, and Hang Xu. Self-adaptive reality-guided diffusion for artifact-free super-resolution. In *Proceedings of the IEEE/CVF Conference on Computer Vision and Pattern Recognition (CVPR)*, pages 25806–25816, June 2024.
- [85] Jie Long Lee, Chen Li, and Gim Hee Lee. Disr-nerf: Diffusion-guided view-consistent super-resolution nerf. In *Proceedings of the IEEE/CVF Conference on Computer Vision and Pattern Recognition (CVPR)*, pages 20561–20570, June 2024.
- [86] Yufei Wang, Wenhan Yang, Xinyuan Chen, Yaohui Wang, Lanqing Guo, Lap-Pui Chau, Ziwei Liu, Yu Qiao, Alex C. Kot, and Bihan Wen. Sinsr: Diffusion-based image super-resolution in a single step. In *Proceedings of the IEEE/CVF Conference on Computer Vision and Pattern Recognition (CVPR)*, pages 25796–25805, June 2024.
- [87] Li Li, Chenwei Wang, You Qin, Wei Ji, and Renjie Liang. Biased-predicate annotation identification via unbiased visual predicate representation. In *Proceedings of the 31st ACM International Conference on Multimedia*, pages 4410–4420, 2023.
- [88] Longguang Wang, Juncheng Li, Yingqian Wang, Qingyong Hu, and Yulan Guo. Learning coupled dictionaries from unpaired data for image super-resolution. In *Proceedings of the IEEE/CVF Conference on Computer Vision and Pattern Recognition (CVPR)*, pages 25712–25721, June 2024.
- [89] Chenwei Wang, Xin Chen, You Qin, Siyi Luo, Yulin Huang, Jifang Pei, and Jianyu Yang. Unveiling causalities in sar atr: A causal interventional approach for limited data. *IEEE Geoscience and Remote Sensing Letters*, 21:1–5, 2024.
- [90] Cunyi Yin, Chenwei Wang, Zhaoke Huang, Hao Jiang, Jing Chen, Xiren Miao, Shaocong Zheng, Jianfei Yang, Zhiwen Chen, Zhenghua Chen, et al. Ciuav: Scalable device-free indoor uav localization via multi-objective optimized network using channel state information. *IEEE Internet of Things Journal*, 2026.
- [91] Chang Qiao, Di Li, Yuting Guo, Chong Liu, Tao Jiang, Qionghai Dai, and Dong Li. Evaluation and development of deep neural networks for image super-resolution in optical microscopy. *Nature Methods*, 18(2):194–202, Feb 2021.
- [92] Boyi Huang, Jia Li, Bowen Yao, Zhigang Yang, Edmund Y. Lam, Jia Zhang, Wei Yan, and Junle Qu. Enhancing image resolution of confocal fluorescence microscopy with deep learning. *PhotoniX*, 4(1):2, Jan 2023.
- [93] Cunyi Yin, Zhaoke Huang, Hao Jiang, Jing Chen, Zhida WANG, Chenwei Wang, Zhenghua Chen, Zhiwen Chen, and Hong Yan. A spatio-temporal feature distribution network for device-free power inspection activity using wifi csi. *IEEE Transactions on Industrial Informatics*, 2025.
- [94] Chang Qiao, Yunmin Zeng, Quan Meng, Xingye Chen, Haoyu Chen, Tao Jiang, Rongfei Wei, Jiabao Guo, Wenfeng Fu, Huaide Lu, Di Li, Yuwang Wang, Hui Qiao, Jiamin Wu, Dong Li, and Qionghai Dai. Zero-shot learning enables instant denoising and super-resolution in optical fluorescence microscopy. *Nature Communications*, 15(1):4180, May 2024.
- [95] Ji Liu, Przemyslaw Musalski, Peter Wonka, and Jieping Ye. Tensor completion for estimating missing values in visual data. 2012.
- [96] Silvia Gandy, Benjamin Recht, and Isao Yamada. Tensor completion and low-n-rank tensor recovery via convex optimization. *Inverse problems*, 27(2):025010, 2011.
- [97] Prateek Jain and Sewoong Oh. Provable tensor factorization with missing data. *Advances in Neural Information Processing Systems*, 27, 2014.
- [98] Ledyard R Tucker. Some mathematical notes on three-mode factor analysis. *Psychometrika*, 31(3):279–311, 1966.
- [99] Lieven De Lathauwer, Bart De Moor, and Joos Vandewalle. A multilinear singular value decomposition. *SIAM journal on Matrix Analysis and Applications*, 21(4):1253–1278, 2000.
- [100] Canyi Lu, Xi Peng, and Yunchao Wei. Low-rank tensor completion with a new tensor nuclear norm induced by invertible linear transforms. In *Proceedings of the IEEE/CVF conference on computer vision and pattern recognition*, pages 5996–6004, 2019.
- [101] Marko Filipović and Ante Jukić. Tucker factorization with missing data with application to low-n-rank tensor completion. *Multidimensional systems and signal processing*, 26(3):677–692, 2015.
- [102] Ming Yuan and Cun-Hui Zhang. On tensor completion via nuclear norm minimization. *Foundations of Computational Mathematics*, 16(4):1031–1068, Aug 2016.

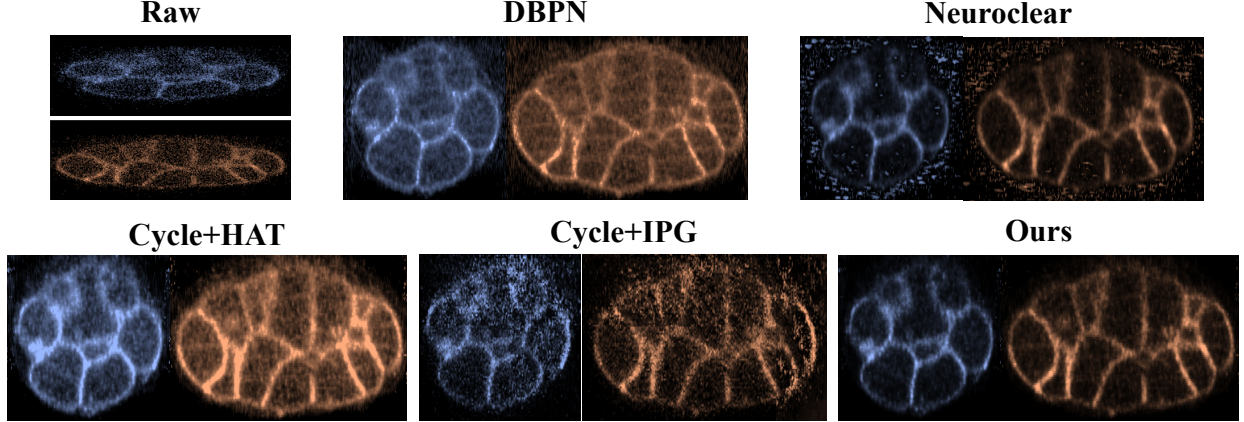


Figure 4: YZ (Yellow) and XZ (Blue) slice qualitative super-resolution comparison of different methods on live 3D fluorescence microscopy volumes at the 2700s time point.

A Detailed Experimental Analysis and More Experimental Validation

Quantitative Comparison with State-of-the-Art Methods.

Table 1 and Table 3 presents a comprehensive comparison of our method against several baselines on SR-CACO-2 and three *in vivo* cellular datasets. On SR-CACO-2, our method achieves the highest PSNR (40.30) and SSIM (0.9476), along with the lowest LPIPS (0.2305), indicating strong pixel-level and perceptual fidelity. Compared to DDPM, which shares a similar generative backbone, our method yields improved perceptual quality (lower LPIPS and higher NRQM) and slightly better structural preservation.

On the more challenging *C. elegans* datasets, our method remains competitive. In dataset 1, while Cycle+IPG achieves the highest NRQM (5.06), it suffers from worse LPIPS (0.3040) and SSIM (0.6338), suggesting potential over-enhancement or structural distortion. Our method provides the best balance between distortion and perceptual quality, with leading SSIM and strong LPIPS and PSNR. In dataset 2, our method again attains the best PSNR (40.95), SSIM (0.9868), and LPIPS (0.2674), outperforming DDPM and Cycle-based baselines by a clear margin.

These results demonstrate that our diffusion-guided approach generalizes well across synthetic and real biological volumes, delivering consistent improvements in both low-level fidelity and perceptual quality.

3D/Slice/Zoom-in Visual Comparison. To comprehensively evaluate the structural fidelity and robustness of our method, we conduct visual comparisons across full 3D reconstructions, individual slices, and zoomed-in regions at two representative time points (2700s and 4950s), as illustrated in Figure 3. Raw observations under low-SNR conditions exhibit severe background noise and blurred or incomplete membrane structures, which hinders morphological interpretation. Bicubic interpolation fails to restore high-frequency details, resulting in oversmoothed textures and edge ambiguity. DBPN, despite leveraging deep residual learning, tends to introduce over-smoothing artifacts and axial distortion due to its reliance on downsampling-upscaling cycles. Unsupervised approaches like Cycle+IPG and Cycle+HAT, although trained without paired data, frequently hallucinate unrealistic structures or distort membrane continuity, especially in low-intensity regions. Neuroclear improves visual sharpness but shows inconsistent local fidelity and introduces background artifacts in some areas. In contrast, our method consistently reconstructs continuous and biologically plausible membrane structures, effectively suppressing noise and restoring fine cellular boundaries. The zoomed-in comparisons clearly reveal our model’s advantage in preserving edge integrity and subcellular continuity across time. These results demonstrate that our diffusion-guided framework generalizes well temporally and is capable of maintaining high spatial fidelity even under challenging acquisition settings.

Performance Statistics Analysis. We further assess the reconstruction quality of our method using quantitative metrics across diverse datasets. Specifically, we evaluate both perceptual and distortion-based performance using LPIPS and PSNR on the SR-CACO-2 dataset and three *C. elegans* volumes. As shown in Figure 8(a), PSNR values remain high and stable across both XY and YZ planes, with SR-CACO-2 showing the highest scores and lowest variance, reflecting relatively clean and uniform structure. The *C. elegans* datasets, which feature higher structural complexity and natural variability, exhibit moderately lower PSNR

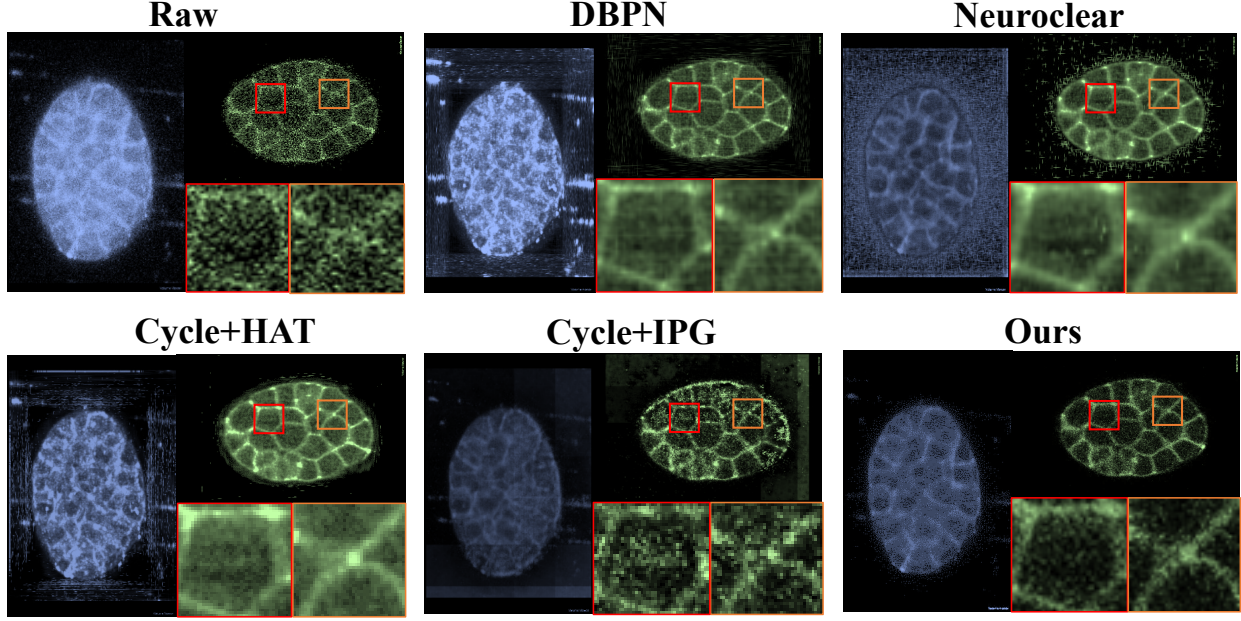


Figure 5: 3D/XY-slice/zoom-in qualitative denoising comparison of different methods on live 3D fluorescence microscopy volumes at the 4950s time point.

values but maintain consistent distributions across both spatial planes. Figure 8(b) shows that LPIPS values are consistently low, indicating strong perceptual similarity to ground truth. SR-CACO-2 again achieves the lowest median LPIPS, while the *C. elegans* datasets show slightly higher scores, likely due to their more heterogeneous and detailed biological morphology. Notably, the similarity of performance between XY and YZ planes across all datasets suggests that our method handles anisotropic imaging characteristics effectively. These quantitative results affirm the generalizability and robustness of our reconstruction framework across both synthetic and real-world biological imaging data.

Temporal Robustness Analysis. To evaluate temporal consistency, we apply our method to reconstruct a dynamic sequence of *in vivo* FM volumes captured between 2700s and 5400s. This time interval corresponds to prolonged imaging under low-SNR conditions, where photon exposure is limited to preserve cell viability. As shown in Figure 9, raw frames progressively degrade in signal quality, with increasing noise and weakening structural clarity. Despite these challenges, our model consistently produces clean and high-fidelity reconstructions over time. Membrane structures remain continuous, and noise accumulation is effectively suppressed, even in later frames with lower signal strength. This demonstrates our method’s robustness against temporal variations in image quality and confirms its applicability in long-term live-cell imaging scenarios where maintaining structural coherence over time is critical.

Rank and Recovery Bound Analysis. We conduct a statistical analysis of tensor rank and observation sufficiency across the dataset to validate the theoretical assumptions underlying our model. Figure 7(a) presents the rank distribution of cell volumes, revealing a bimodal pattern with peaks around ranks 15 and 30. The mean rank is 20.83 with notable variance, reflecting the diverse structural complexity of cellular data. This variability underscores the importance of adaptive rank modeling rather than fixed-rank assumptions in volumetric restoration. Figure 7(b) shows the distribution of the lower observed bound $|\Omega|$ required for exact recovery. Most samples exceed the theoretical threshold for rank 10, suggesting that the empirical observation densities are sufficient to ensure theoretical recoverability. However, the presence of a long-tailed, multimodal distribution also indicates that a subset of samples remains challenging, particularly those with higher rank or less complete observations. These insights justify our design of a flexible, data-aware tensor completion and diffusion framework that can adapt to the structural and observational diversity in real-world fluorescence microscopy data.

Robustness to Noise and Downsampling. Table 2 summarizes the performance of our method under various levels of Gaussian noise and downsampling factors, based on the *C. elegans* evaluation dataset. Starting from clean inputs, we observe a gradual degradation in reconstruction quality as noise intensity

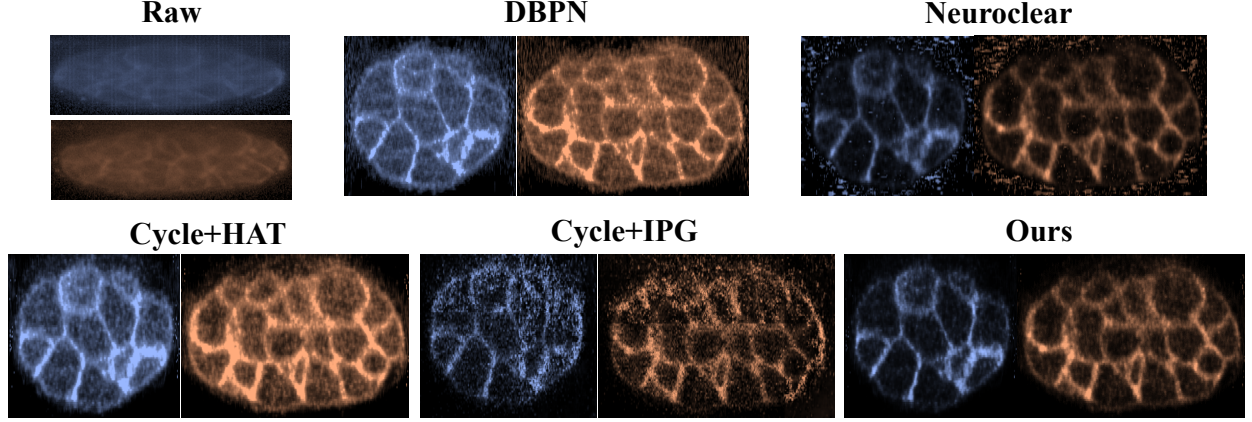


Figure 6: YZ (Yellow) and XZ (Blue) slice qualitative super-resolution comparison of different methods on live 3D fluorescence microscopy volumes at the 4950s time point.

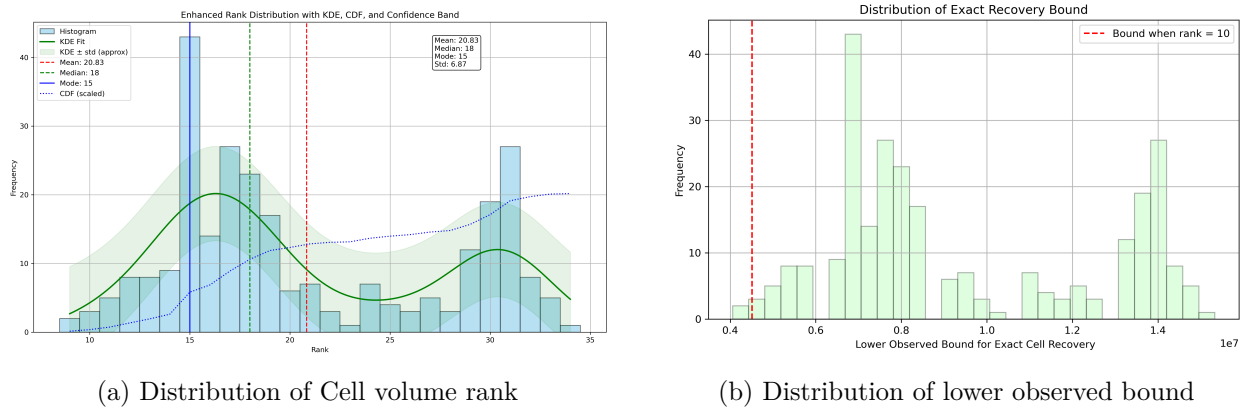


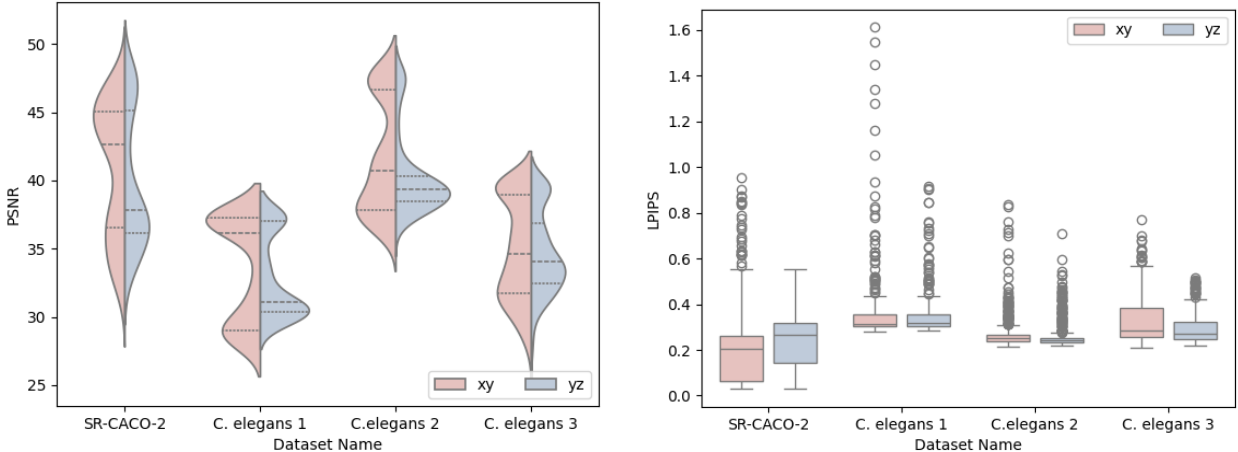
Figure 7: Distributions of cell tensor ranks and lower observed bound $|\Omega|$ for exact cell recovery across the dataset.

increases. PSNR drops from 33.18 (clean) to 29.34 under $\sigma = 0.1$, while SSIM falls accordingly from 0.6682 to 0.5421, reflecting increased structural distortion. LPIPS also rises with noise, indicating reduced perceptual similarity. Meanwhile, NIQE and PIQE, as no-reference metrics, increase consistently, capturing the perceptual degradation introduced by noise. A similar trend is observed with increasing downsampling factors. PSNR and SSIM degrade from 30.53 and 0.6154 at $\times 2$ downsampling to 28.21 and 0.5255 at $\times 4$, respectively. Perceptual quality metrics such as LPIPS and NRQM also indicate reduced fidelity at higher compression levels. Despite these degradations, our method maintains relatively stable performance across all settings, with smooth and interpretable declines. The results demonstrate the robustness of our model under practical imaging degradations, including low-SNR conditions and resolution loss.

Limitations and Future Work. While our method demonstrates strong performance across multiple datasets, it has primarily been evaluated on fluorescence microscopy data. Further validation on other bio-image modalities would help assess generalizability. Additionally, although the current framework shows stable performance under noise and resolution degradation, integrating weak supervision or modality priors may further enhance adaptability. Future work will explore broader dataset coverage, improved robustness, and optimization for computational efficiency.

We also evaluate the temporal robustness of our method using a sequence of *in vivo* fluorescence microscopy images captured over time, from 2700s to 5400s. The raw observations suffer from high noise and degraded structural details due to prolonged imaging under low-SNR conditions. Our method is applied frame-by-frame to reconstruct the clean high-fidelity volume across this time series.

As illustrated in Fig. 9, our method consistently improves structural fidelity and effectively suppresses noise throughout the sequence. Notable enhancements are observed across all frames, with particularly clear



(a) Violin plots of PSNR values for SR-CACO-2 and three *C. elegans* datasets.

(b) LPIPS distributions across XY and YZ planes for SR-CACO-2 and three *C. elegans* datasets.

Figure 8: Performance statistics analysis across XY and YZ planes for SR-CACO-2 and three *C. elegans* datasets.

Table 3: Performance comparison of our method and other methods under SR-CACO-2 and two datasets of in vivo cellular volumes.

Model	PSNR↑	SSIM↑	LPIPS↓	NIQE↓	PIQE↓	NRQM↑
<i>C. elegans</i> evaluation dataset 3						
DBPN	32.84	0.6984	0.3956	16.85	52.91	2.60
Neuroclear	31.51	0.7339	0.3665	16.23	54.00	1.88
Cycle+HAT	33.96	0.8053	0.2077	16.06	48.97	2.09
Cycle+IPG	33.22	0.7881	0.1995	15.36	48.68	2.50
DDPM(Baseline)	33.43	0.8037	0.1986	15.94	53.48	2.24
Ours	34.81	0.8174	0.1168	12.11	47.53	2.97

improvements from 2700s to 5400s. This demonstrates the model’s ability to maintain stable and reliable reconstruction performance under challenging conditions and over extended temporal acquisition periods. The results validate the temporal consistency and robustness of our diffusion-guided reconstruction framework.

B Motivation

Cell division is one of the most fundamental processes of life—it drives growth and reproduction, yet also sets the stage for aging and death [1, 2]. Understanding this process at the structural level is crucial for advancing research in areas such as developmental biology, oncology, and regenerative medicine. Observing the 3D membrane structure of cells during live cell division is especially important, as the membrane plays a central role in maintaining cellular integrity and mediating dynamic interactions [4]. This observation typically involves volumetric scanning along the Z-axis, where high-resolution XY-plane images are acquired at equidistant depths with the help of fluorescent dyes.

To minimize lethal phototoxicity during this process, the scanning time must be strictly limited, reducing the number of axial slices and the overall imaging intensity. As a result, 3D live-cell imaging often suffers from anisotropic resolution and spatially varying noise, particularly in deeper or faster-acquired slices, as illustrated in Fig. 1. These constraints significantly limit the spatial-temporal fidelity of the captured volumes, making

Table 4: Super-resolution performance on the SR-CACO-2 test set (full image).

SISR Method	PSNR (↑)				NRMSE (↓)				SSIM (↑)			
	CELL0	CELL1	CELL2	Mean	CELL0	CELL1	CELL2	Mean	CELL0	CELL1	CELL2	Mean
Bicubic	41.76	38.22	37.07	39.02	0.0383	0.0286	0.0337	0.0335	0.9470	0.9233	0.9128	0.9277
Pre-upsampling SR												
SRCNN [42]	37.59	37.39	36.99	37.33	0.0650	0.0319	0.0340	0.0436	0.7103	0.8157	0.8419	0.7893
VDSR [43]	43.14	39.08	38.53	40.25	0.0312	0.0251	0.0279	0.0281	0.9611	0.9418	0.9381	0.9470
DRRN [44]	43.14	39.03	38.43	40.20	0.0310	0.0253	0.0282	0.0282	0.9623	0.9408	0.9364	0.9465
MemNet [45]	41.39	36.23	36.89	38.17	0.0390	0.0374	0.0345	0.0370	0.9463	0.7588	0.9096	0.8716
Post-upsampling SR												
NLSN [46]	39.59	38.12	37.40	38.37	0.0505	0.0286	0.0324	0.0372	0.7986	0.8816	0.8756	0.8519
DFCAN [47]	43.19	39.12	38.26	40.19	0.0307	0.0250	0.0287	0.0281	0.9641	0.9422	0.9194	0.9419
SwinIR [48]	42.00	38.73	38.23	39.65	0.0347	0.0263	0.0291	0.0300	0.9257	0.9238	0.9266	0.9253
EDSR [49]	37.48	36.80	37.81	37.36	0.0656	0.0335	0.0289	0.0427	0.7034	0.8008	0.9323	0.8122
ENLCN [50]	40.03	38.33	37.74	38.70	0.0476	0.0278	0.0309	0.0354	0.8221	0.8929	0.8946	0.8699
GRL [51]	41.74	36.18	37.60	38.50	0.0370	0.0374	0.0311	0.0351	0.9115	0.7372	0.8681	0.8389
ACT [52]	39.07	36.76	35.36	37.07	0.0542	0.0345	0.0420	0.0436	0.7717	0.7813	0.7411	0.7647
Omni-SR [53]	42.14	38.63	37.94	39.57	0.0352	0.0265	0.0301	0.0306	0.9488	0.9313	0.9209	0.9337
Iterative up-and-down sampling SR												
DBPN [54]	37.87	38.19	35.96	37.34	0.0634	0.0284	0.0386	0.0435	0.7108	0.8772	0.7735	0.7871
SRFBN [55]	42.24	38.20	37.07	39.17	0.0358	0.0286	0.0339	0.0328	0.9498	0.8993	0.8802	0.9098
Progressive upsampling SR												
ProSR [56]	41.65	38.61	38.08	39.45	0.0376	0.0267	0.0295	0.0313	0.9050	0.9044	0.9095	0.9063
MS-LapSRN [57]	30.99	31.81	33.69	32.16	0.1277	0.0657	0.0493	0.0809	0.4628	0.5500	0.6905	0.5678
Ours	41.59	38.47	40.98	40.30	0.0228	0.0276	0.0198	0.0254	0.9581	0.9348	0.9562	0.9475

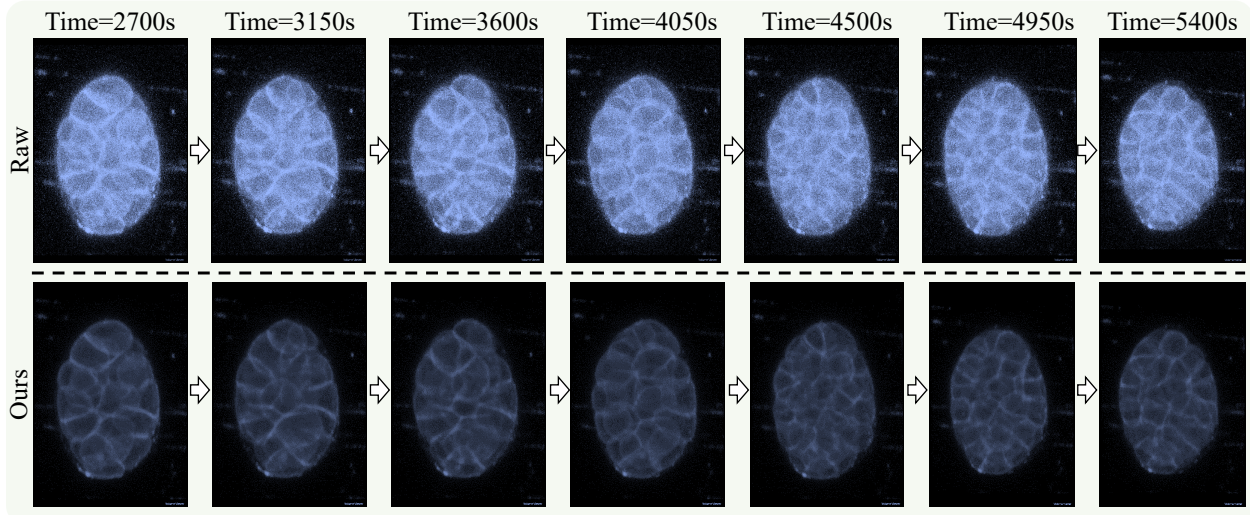


Figure 9: Temporal comparison of raw observations and our reconstructed results at multiple time points. The proposed method consistently enhances structural fidelity and suppresses noise over time, particularly under challenging low-SNR conditions. Improvements are evident from 2700s to 5400s, demonstrating the robustness of our diffusion-guided reconstruction across the temporal sequence.

it difficult to reconstruct fine membrane structures or dynamic changes. This, in turn, impedes fundamental insights in a wide range of biomedical fields [5, 3].

FM imaging involves a sophisticated and multi-stage imaging process that includes light source excitation, fluorescent signal emission from labeled samples, and diffraction and detection through optical elements such as objective lenses and detectors [22, 58]. Each stage introduces its own set of nonlinearities and complexities, which are further compounded by intricate interactions between light and biological tissue—such as multiphoton absorption, scattering, and refractive index mismatches [23]. These interactions distort the original signal in ways that are difficult to model analytically. In addition, practical imaging conditions introduce significant noise sources, including optical noise from detectors, autofluorescence from surrounding tissues, and background interference from out-of-focus regions. Particularly in live-cell imaging, low excitation power is required to minimize phototoxicity, resulting in low signal-to-noise ratios (SNR), especially under fast volumetric scanning or time-lapse acquisition [31, 59]. Compounding these challenges, the biological structures being imaged are often highly heterogeneous and dynamic, leading to signal attenuation, scattering, and partial transmission that result in spatially incomplete or missing data [32]. These issues collectively render the fluorescence microscopy (FM) imaging process highly nonlinear, noisy, and partially observable. An overview of this process is illustrated in Fig. 1.

Inverse problem-based methods have been widely adopted to restore degraded images by mathematically modeling the imaging process as a forward degradation operator and estimating its inverse. However, such methods typically rely on simplified assumptions—most often that the degradation is linear, spatially invariant, and governed by known and stable physical models [26, 25]. These assumptions may hold in well-controlled synthetic settings, but they fall short in the context of FM imaging. The nonlinear optical transfer functions, sample-dependent variability, and the unpredictable effects of biological environments render inverse formulations insufficient to capture the true complexity of FM imaging. Moreover, under realistic conditions characterized by low SNR and sparse observations, these inverse problems become severely ill-posed: small variations or noise in the input can lead to disproportionately large errors in the output, making the reconstruction process unstable and unreliable. As a result, obtaining high-quality, artifact-free reconstructions using traditional inverse approaches is extremely difficult—an issue particularly critical for life science applications, where precise structural fidelity is essential for downstream analysis and biological interpretation, as highlighted in Fig. 1.

C Related Work

C.1 Deep Learning Driven image restoration

Deep learning has revolutionized single-image super-resolution (SR) by introducing architectures that jointly improve image fidelity and computational throughput. Early convolutional neural network (CNN) approaches such as SRCNN demonstrated that end-to-end feature learning can outperform traditional interpolation [8], while deeper architectures like VDSR showed that residual learning facilitates faster convergence and higher peak signal-to-noise ratios [60, 61]. Subsequent models, for instance EDSR, removed unnecessary components to streamline performance on high-resolution (HR) reconstruction tasks [62, 63, 64].

Building on these foundations, attention-augmented CNNs learned to prioritize salient image regions, refining perceptual details and structural consistency [65, 66, 67]. Generative adversarial networks (GANs) further advanced SR by introducing a discriminative component that drives the generator to synthesize realistic textures and fine-scale details, leading to more visually convincing outputs [68, 69, 70, 71]. More recently, Transformers have introduced long-range dependency modeling, improving feature representation and global context learning [72, 73, 74, 75, 76, 77, 78]. IPT [72] showcased the potential of large-scale pre-trained Transformers, while SwinIR [76, 79] leveraged hierarchical Swin Transformers [80, 81, 82] for multi-scale processing.

Beyond these architectures, emerging directions in SR research include graph-based methods that encode pixel relationships as graph structures [83], diffusion probabilistic models that iteratively refine noisy estimations [84, 85, 86, 87], and dictionary-learning approaches that learn sparse representations for reconstruction [88, 89]. While these techniques offer promising gains, they often demand extensive paired datasets or encounter stability challenges during training. As the field advances, ongoing work aims to enhance data efficiency, robustness to diverse degradations, and runtime efficiency to bridge the gap between research prototypes and deployable SR systems [90].

C.2 SR of 3D Fluorescence Microscopy

Achieving super-resolution in 3D fluorescence microscopy remains challenging due to anisotropic optical blurring and low signal-to-noise ratios. A range of deep learning approaches has been proposed to tackle these issues by exploiting both spatial and frequency-domain priors. For instance, DFCAN [91] employs a multi-scale frequency extraction module to recover fine structural details, while OT-CycleGAN [17] integrates 3D optimal-transport objectives into an adversarial framework to enforce isotropic resolution restoration. Self-Net [15] takes advantage of inherent high-resolution lateral views by learning a cross-axis mapping that refines axial detail. In parallel, TCAN [92] introduces a dual-channel attention mechanism that selectively emphasizes informative features from both spatial and channel dimensions. More recently, SN2N [16] adopts a self-supervised Noise2Noise strategy to denoise and upsample without ground-truth high-resolution volumes, improving robustness across imaging modalities [93].

Despite these advances, many methods underuse the rich structural priors present in 3D cellular data. A notable example is the SimCLR-inspired model by Qiao et al. [94], which jointly learns denoising and super-resolution objectives but falls short in fully leveraging volumetric context, leading to occasional instability and less accurate reconstructions. A detailed comparison is provided in the experimental section.

C.3 Tensor Completion and Tucker Decomposition

In recent years, recovering high-dimensional data from incomplete or damaged observations has become a key challenge. Tensor completion generalizes the matrix completion problem to higher-order arrays by exploiting low-rank structure across multiple modes. The field was catalyzed by the success of low-rank matrix completion via nuclear-norm minimization, which proved that one can exactly recover a low-rank matrix from a small subset of its entries. Building on this foundation, early work extended convex relaxation to tensors. [95] introduced the early definition of a tensor trace norm (as the sum of nuclear norms of matricizations) and formulated tensor completion as a convex program. They developed effective algorithms - e.g. Simple, Fast, and High-accuracy Low-Rank Tensor Completion (SiLRTC, FaLRTC, HaLRTC) - to solve tensor trace-norm minimization in visual data. [96] likewise proposed recovering a “low-n-rank” tensor (low rank in every mode) via convex optimization, treating the multi-dimensional case as a natural extension of matrix completion. These seminal methods demonstrated that missing entries in multi-way data (images, videos, etc.) can be accurately imputed by enforcing low multilinear rank. Beyond convex approaches, researchers explored direct factorization strategies. For example, [97] proposed an alternating least-squares scheme (analogous to CP decomposition) with provable guarantees, showing that Under the standard μ -incoherence assumption, we prove that through the alternating minimization algorithm, only $O(\mu^6 r^5 n^{3/2} (\log n)^4)$ random observations are needed to uniquely and exactly reconstruct a rank- r orthogonal third-order tensor. Such developments - spanning convex relaxations and nonconvex alternating optimization - have established tensor completion as a rich research area.

The Tucker decomposition provides a foundational model for multi-way low-rank structure, essentially serving as a higher-order form of PCA. First introduced by [98] as three-mode factor analysis and later formalized as the higher-order SVD (HOSVD) by [99]. Tucker decomposition expresses a tensor as a small core tensor multiplied by orthogonal factor matrices along each mode. This multilinear factorization was soon leveraged in tensor completion to enforce low Tucker rank. Early convex approaches implicitly used Tucker’s idea by minimizing the nuclear norms of unfolded tensors - the closest convex proxy to Tucker rank [100]. While such relaxations are theoretically appealing, an alternate line of work directly applied Tucker factorization to incomplete tensors. For instance, [101] proposed an ALS-based Tucker decomposition algorithm for tensor completion, showing it can recover tensors even when the assumed ranks are higher or lower than the true ranks. Their Tucker-based method was demonstrated to outperform nuclear-norm minimization approaches when only a very small fraction of entries is observed, underscoring Tucker’s practical efficacy in extremely sparse settings. In parallel, optimization on the manifold of fixed multilinear rank tensors has been developed to handle Tucker models efficiently. [38] introduced a Riemannian conjugate gradient scheme on the manifold of tensors of fixed Tucker rank, achieving scalable performance and accurate recovery even when the vast majority of entries are missing. The Tucker decomposition’s solid theoretical basis - capturing multi-mode interactions via a core tensor - and its strong empirical performance (e.g. in image inpainting and hyperspectral data recovery) have made it a cornerstone in tensor completion research. By combining Tucker’s multi-linear algebra principles with modern optimization techniques, these works have significantly advanced the state-of-the-art, offering methods with both deep theoretical guarantees and high practical impact in multi-dimensional data reconstruction.

D Generalization vs Specificity

In this section, we provide a detailed discussion to clarify the motivation, scope, and implications of adopting structural priors in our model, in response to concerns about the generality and applicability of our approach.

Motivation for Structural Priors in Biological Imaging. Unlike general-purpose image restoration tasks where input data may exhibit highly diverse and unstructured content, our work focuses on fluorescence microscopy (FM) imaging of model cellular systems, particularly epithelial cell lines like Caco-2. These cells are known to exhibit strong morphological regularities, such as rounded membrane contours and consistent spatial organization across samples. These regularities are not incidental, but instead rooted in biological mechanisms such as cell polarity and tissue architecture.

Given this domain-specific consistency, incorporating a structural prior is not only reasonable but also scientifically motivated. It enables the model to leverage biologically meaningful constraints, reducing noise-induced ambiguity and promoting faithful recovery of cellular morphology—critical for downstream tasks such as segmentation, tracking, and mitotic spindle orientation analysis.

Trade-Off Between Generality and Reliability. We acknowledge that structural priors learned from the training data may not generalize well to arbitrarily structured images outside the cellular domain. However, our design intentionally sacrifices some degree of generality in favor of domain-specific reliability. In cellular imaging, even minor geometric distortions can compromise biological interpretation. Therefore, we prioritize structural fidelity over universal applicability.

Moreover, general models that assume arbitrary structures often introduce randomness or deformation in the restored outputs, particularly under heavy noise or undersampling. This can severely limit their utility in biomedical contexts, where precision and reproducibility are essential.

Domain-Specific Applicability and Broader Value. It is important to emphasize that our method is designed for a specific yet widely relevant domain: long-term FM imaging of model organisms in biomedical research. While it may not apply to all imaging domains, it holds significant value within its intended scope. For example, Caco-2 and similar epithelial cell lines are broadly used in drug testing, cell biology, and tissue engineering, where consistent structural modeling is highly advantageous.

Thus, our use of structural priors is a principled design choice aligned with the characteristics and needs of this domain, rather than an arbitrary or overly narrow constraint. Future extensions may explore ways to adaptively relax the prior or incorporate uncertainty modeling to broaden applicability.

E Proof of Exact Tensor Completion Requirement

E.1 Exact Recovery Guarantee for Incoherent Tensor Completion

We restate the recovery problem

$$\min_{\mathcal{X}} \|\mathcal{X}\|_* \quad \text{s.t.} \quad \mathcal{P}_\Omega(\mathcal{X}) = \mathcal{P}_\Omega(\mathcal{T}), \quad (2)$$

and prove that *uniform* sampling with

$$|\Omega| = \mathcal{O}((rI^{3/2} + r^2I)\log^2 I)$$

is sufficient for exact recovery with high probability.

Let T be the tangent space at \mathcal{T} in Tucker format and Q_T , Q_T^\perp the orthogonal projections onto T and T^\perp . Define

$$\mu_* = \frac{d_*^k}{kr_*^{k-1}d} \max_{i_1, \dots, i_k} \|Q_T(e_{i_1} \otimes \dots \otimes e_{i_k})\|_{\text{HS}}^2, \quad r_* = \left[\frac{1}{kd} \sum_{j=1}^k \frac{I_j}{r_j} \prod_{\ell} r_\ell \right]^{1/(k-1)},$$

and $\alpha_* = (d_*^k/r_*)^{1/2} \|W_0\|_{\text{max}}$, where W_0 is a sub-gradient of $\|\mathcal{T}\|_*$. The *incoherence constraint* requires $\mu_* = \mathcal{O}(1)$, $\alpha_* = \mathcal{O}(1)$. Here, k is the tensor order, $I = \max_j I_j$ is the maximal mode dimension, $r = \max_j r_j(\mathcal{T})$ is the maximal Tucker rank, $d = \frac{1}{k} \sum_j I_j$ is the arithmetic mean and $d_* = (\prod_j I_j)^{1/k}$ is the geometric mean.

Lemma 1 (sufficient condition) *If there exists $\tilde{\mathcal{G}} \in \text{Range}(\mathcal{P}_\Omega)$ such that*

$$\|Q_T(\tilde{\mathcal{G}} - W_0)\|_{\text{HS}} \leq \frac{\sqrt{n/(2d_*^k)}}{k(k-1)}, \quad (\text{A1})$$

$$\|Q_T^\perp \tilde{\mathcal{G}}\|_* < 1 - \frac{1}{k(k-1)}, \quad (\text{A2})$$

$$\|Q_T\left(\frac{d_*^k}{n}\mathcal{P}_\Omega - \mathcal{I}\right)Q_T\|_{\text{HS} \rightarrow \text{HS}} \leq \frac{1}{2}, \quad (\text{A3})$$

then the minimiser of (2) is unique and equals \mathcal{T} .

The proof is a direct adaptation of Lemma 1 in [102], which proceeds in three key steps.

Step 1: Sampling Operator Concentration

For Ω sampled without replacement,

$$\mathbb{P}\{\|Q_T\left(\frac{d_*^k}{n}\mathcal{P}_\Omega - \mathcal{I}\right)Q_T\|_{\text{HS} \rightarrow \text{HS}} \geq \tau\} \leq 2k r_*^{k-1} d \exp\left[-\frac{\tau^2/2}{1+2\tau/3} \frac{n}{k\mu_* r_*^{k-1} d}\right].$$

Setting $\tau = \frac{1}{2}$ and demanding the RHS $\leq I^{-\beta}$ yields

$$n \gtrsim c_k(\beta+1) \mu_* r_*^{k-1} d \log I. \quad (\text{B})$$

Step 2: Golfing-Scheme Construction

Split $\Omega = \biguplus_{j=1}^{n_2} \Omega_j$ with $|\Omega_j| = n_1$ (so $n = n_1 n_2$) and define

$$\mathcal{R}_j = \mathcal{I} - \frac{d_*^k}{n_1} \sum_{\omega \in \Omega_j} \mathcal{P}_\omega, \quad \mathcal{W}_0 = W_0, \quad \mathcal{W}_j = Q_T \mathcal{R}_j Q_T \mathcal{W}_{j-1}.$$

The candidate dual certificate is $\tilde{\mathcal{G}} = \sum_{j=1}^{n_2} (\mathcal{I} - \mathcal{R}_j) \mathcal{W}_{j-1}$.

Tangent-space contraction. By matrix Bernstein,

$$\|\mathcal{W}_j\|_{\text{HS}} \leq \tau^j \|W_0\|_{\text{HS}} \quad \text{with} \quad \tau = \sqrt{\frac{k\mu_* r_*^{k-1} d \log I}{n_1}}.$$

Choose $n_1 = c_1 \mu_* r_*^{k-1} d \log I$ so $\tau = \frac{1}{2}$. Taking $n_2 = c_2 \log I$ ensures Eq. (A1).

Orthogonal-space leakage. For the max-norm we invoke Lemma 3.3 of [102]: with $n_1 \gtrsim r^{(k-1)/2} I^{3/2} \log I$ and $n_2 \asymp \log I$, condition Eq. (A2) is satisfied with high probability.

Step 3: Sample-Size Consolidation

Combine the two requirements on n_1, n_2 :

$$n = n_1 n_2 \gtrsim (\mu_* + \alpha_*^2 \lambda_*^{k-2}) r_*^{k-1} I (\log I)^2 + \alpha_* \lambda_*^{k/2-1} r_*^{(k-1)/2} I^{3/2} (\log I)^2.$$

Under the mild-incoherence regime $\mu_* = \alpha_* = \lambda_* = \mathcal{O}(1)$ and $r_* = \Theta(r)$, this simplifies (for $k = 3$) to

$$n = \mathcal{O}((rI^{3/2} + r^2 I) \log^2 I),$$

completing the proof. ■

E.2 Exact Recovery Guarantee for Robust Tensor Completion

We extend the dual-certificate argument of **(author?)** [102] to the robust setting where the observation $\mathcal{T} = \mathcal{X} + \mathcal{E}$ contains a low-rank component \mathcal{X} and an entry-wise sparse component \mathcal{E} .

Step 1: Dual Programme. The Lagrangian of (3) is

$$\mathcal{L}(\mathcal{X}, \mathcal{E}, \mathcal{G}) = \|\mathcal{X}\|_* + \lambda_1 \|\mathcal{E}\|_1 + \langle \mathcal{G}, \mathcal{P}_\Omega(\mathcal{X} + \mathcal{E} - \mathcal{Y}) \rangle,$$

with dual constraint $\mathcal{P}_\Omega(\mathcal{G}) = \mathcal{G}$, $\|\mathcal{P}_T(\mathcal{G})\|_2 \leq 1$, $\|\mathcal{P}_{T^\perp}(\mathcal{G})\|_\infty \leq \lambda_1$. Exact recovery is guaranteed if we can find a dual certificate $\tilde{\mathcal{G}}$ satisfying the above constraints and $\mathcal{P}_T \tilde{\mathcal{G}} = W_0$, $\mathcal{P}_\Omega \tilde{\mathcal{G}} = \tilde{\mathcal{G}}$.

Step 2: Golfing Scheme. Split the sample set $\Omega = \biguplus_{\ell=1}^L \Omega_\ell$, $|\Omega_\ell| = m$ and define recursively

$$\mathcal{W}_0 = W_0, \quad \mathcal{W}_\ell = Q_T \left(\mathcal{I} - \frac{d_*^k}{m} \sum_{\omega \in \Omega_\ell} \mathcal{P}_\omega \right) Q_T \mathcal{W}_{\ell-1}.$$

$$\text{Set } \tilde{\mathcal{G}} = \sum_{\ell=1}^L \left(\mathcal{I} - \frac{d_*^k}{m} \sum_{\omega \in \Omega_\ell} \mathcal{P}_\omega \right) \mathcal{W}_{\ell-1}.$$

Step 3: Control on the Tangent Space. Matrix–Bernstein gives

$$\|\mathcal{W}_\ell\|_{\text{HS}} \leq \left(\frac{1}{2} \right)^\ell \|W_0\|_{\text{HS}} \quad \text{if } m \gtrsim \mu r^{k-1} I \log I.$$

With $L = \Theta(\log I)$ we have $\|\mathcal{P}_T(\tilde{\mathcal{G}} - W_0)\|_{\text{HS}} \leq I^{-\beta}$.

Step 4: Control on the Orthogonal Space and Sparsity. For any fixed tensor \mathcal{Z} with $\|\mathcal{P}_{T^\perp} \mathcal{Z}\|_\infty \leq 1$ and $\text{supp}(\mathcal{Z}) \subseteq \Omega$, Hoeffding–type bounds yield

$$\langle \mathcal{P}_{T^\perp} \tilde{\mathcal{G}}, \mathcal{Z} \rangle \leq c_1 \sqrt{\frac{\log I}{m}} = O(I^{-\beta}),$$

provided $m \gtrsim I^{3/2} r^{(k-1)/2} \log I$. Since the support of \mathcal{E} is uniformly random and of size s , a union bound ensures $\|\mathcal{P}_{T^\perp} \tilde{\mathcal{G}}\|_\infty \leq \lambda_1$ as long as $m \gtrsim s \log I$.

Step 5: RIP on Sparse Part. Define \mathcal{P}_S as the projection onto entries in $S = \text{supp}(\mathcal{E})$. Standard coupon–collector arguments give

$$\left\| \frac{d_*^k}{n} \mathcal{P}_\Omega \mathcal{P}_S - \mathcal{P}_S \right\|_{2 \rightarrow 2} \leq \frac{1}{2} \implies n \gtrsim s \log I.$$

Step 6: Collecting Bounds. Pick m to satisfy simultaneously

1. $m \gtrsim \mu r^{k-1} I \log I$;
2. $m \gtrsim r^{(k-1)/2} I^{3/2} \log I$;
3. $m \gtrsim s \log I$.

With $L = \Theta(\log I)$ the total sample size $n = mL$ obeys

$$|\Omega| = \mathcal{O}((r^{k-1} I + r^{(k-1)/2} I^{3/2} + s) \log^2 I).$$

For the most common case $k = 3$ this becomes $|\Omega| = \mathcal{O}((r^2 I + r I^{3/2} + s) \log^2 I)$. Absorbing constants and taking $r = \max_j r_j$ gives

$$|\Omega| \geq C(r I^{3/2} + s) \log^2 I,$$

completing the proof. \square

F Proposed Solution: Tucker Decomposition-based Tensor Completion

This section provides the alternating-direction method of multipliers (ADMM) that we use to tackle the robust tensor-completion objective in Eq. (3). We first motivate *why* Tucker decomposition and ADMM are natural partners for fluorescence volumes, then guide the reader through every mathematical step—sprinkling each derivation. We close with a convergence theorem and a fully annotated algorithm.

F.1 Why Tucker, and Why ADMM?

Fluorescence microscopy (FM) data contain two complementary structures:

1. a *global, low-rank backbone* that reflects optical blur and the smooth nature of biological tissue; and
2. *sporadic, high-amplitude outliers* triggered by photon shot noise and electronic glitches.

Tucker decomposition excels at capturing the backbone with a tiny core \mathcal{G} and three thin mode matrices $U^{(n)}$. ADMM, in turn, lets us peel the two structures apart by alternating between a *low-rank projection* (to refine the backbone) and a *sparse shrinkage* (to trap outliers). The result is a solver that is *both* mathematically transparent and computationally light-weight.

F.2 Problem in Tucker Coordinates

Denote by Ω the set of measured voxels and by \mathcal{P}_Ω the projection that keeps only those entries. We assume

$$\mathcal{Z} = \mathcal{G} \times_1 U^{(1)} \times_2 U^{(2)} \times_3 U^{(3)}, \quad U^{(n)\top} U^{(n)} = \mathbf{I}_{r_n},$$

where the ranks $\mathbf{r} = (r_1, r_2, r_3)$ satisfy $r_n \ll I_n$. The robust-completion objective becomes

$$\begin{aligned} & \min_{\mathcal{G}, \{U^{(n)}\}, \mathcal{E}} \frac{1}{2} \|\mathcal{G}\|_F^2 + \lambda_1 \|\mathcal{E}\|_1 \\ & \text{s.t. } \mathcal{P}_\Omega(\mathcal{Z} + \mathcal{E}) = \mathcal{Y}_\Omega, \quad \mathcal{Z} \geq 0. \end{aligned} \quad (21)$$

F.3 Augmented Lagrangian

To transform the hard equality constraint into something we can iterate on, introduce a dual tensor Λ and a penalty weight $\rho > 0$:

$$\mathcal{L}_\rho = \frac{1}{2} \|\mathcal{G}\|_F^2 + \lambda_1 \|\mathcal{E}\|_1 + \langle \Lambda, \mathcal{P}_\Omega(\mathcal{Z} + \mathcal{E} - \mathcal{Y}) \rangle + \frac{\rho}{2} \|\mathcal{P}_\Omega(\mathcal{Z} + \mathcal{E} - \mathcal{Y})\|_F^2. \quad (22)$$

The quadratic term is an increasingly strict ‘‘penalty fence’’ driving the iterates toward data fidelity, while Λ records mismatch information for the next cycle.

F.4 ADMM Updates

Initialize $\mathcal{Z}^{(0)} = \mathcal{P}_\Omega(\mathcal{Y})$, $\mathcal{E}^{(0)} = 0$, and $\Lambda^{(0)} = 0$. Each outer loop then performs five conceptually clear acts.

Step 1: Core tensor $\mathcal{G}^{(t+1)}$. Fix $\{U^{(n)}\}, \mathcal{E}^{(t)}, \Lambda^{(t)}$. Using the mode-1 unfolding $\mathcal{Z}_{(1)} = U^{(1)} \mathcal{G}_{(1)} (U^{(3)} \odot U^{(2)})^\top$, solve

$$(\mathbf{I} + \rho \Gamma^\top \Gamma) \mathcal{G}_{(1)}^{(t+1)} = \rho \Gamma^\top \Xi_{(1)}, \quad \Gamma = U^{(1)\top} \mathcal{P}_{\Omega(1)}(U^{(3)} \odot U^{(2)}),$$

where $\Xi = \mathcal{P}_\Omega(\mathcal{Y} - \mathcal{E}^{(t)} - \Lambda^{(t)})$. Modes 2 and 3 have identical structure; all systems are size $r_n \times r_n$.

Step 2: Factor matrices $U^{(n)}$. For each $n \in \{1, 2, 3\}$,

$$\min_{U^\top U = \mathbf{I}} \|\Xi_{(n)} - \rho^{-1} \Lambda_{(n)} - U \mathcal{G}_{(n)}^{(t+1)} (U^{(3)} \odot U^{(2)})^\top\|_F^2. \quad (23)$$

Let $M = (\Xi_{(n)} - \rho^{-1} \Lambda_{(n)}) (U^{(3)} \odot U^{(2)}) \mathcal{G}_{(n)}^{(t+1)\top}$, compute $\text{SVD}(M) = P \Sigma Q^\top$, and set $U^{(n)} = P Q^\top$ (orthogonal Procrustes).

Step 3: Sparse tensor $\mathcal{E}^{(t+1)}$.

$$\mathcal{E}^{(t+1)} = \text{SoftThreshold}_{\lambda_1/\rho}(\mathcal{Y}_\Omega - \mathcal{Z}_\Omega^{(t+1)} - \Lambda^{(t)}),$$

applied *only* on observed entries.

Step 4: Dual tensor.

$$\Lambda^{(t+1)} = \Lambda^{(t)} + \mathcal{P}_\Omega(\mathcal{Z}^{(t+1)} + \mathcal{E}^{(t+1)} - \mathcal{Y}).$$

Step 5: Reconstruction.

$$\mathcal{Z}^{(t+1)} = \mathcal{G}^{(t+1)} \times_1 U^{(1)} \times_2 U^{(2)} \times_3 U^{(3)}.$$

One full sweep costs core LS $\mathcal{O}(r_1 r_2 r_3 + |\Omega|)$, three Procrustes updates $\sum_n \mathcal{O}(I_n r_n^2)$, and residual operations $\mathcal{O}(|\Omega|)$.

F.5 Convergence

Theorem 3 (Global Convergence) *If $|\Omega| \geq C(r I^{3/2} + s) \log^2 I$ and the restricted-isometry conditions in Theorem 2 hold, then the ADMM sequence $(\mathcal{Z}^{(t)}, \mathcal{E}^{(t)}, \Lambda^{(t)})$ converges to the unique global minimiser $(\mathcal{X}^*, \mathcal{E}^*)$ of Eq. (21).*

Sketch. Each sub-problem is convex with a unique minimiser; two-block ADMM theory plus a dual-certificate guarantees convergence.

F.6 Implementation

Algorithm 1 translates the math into code-ready steps.

Algorithm 1 ADMM for Robust Tucker Completion

Require: Observation \mathcal{Y} , mask Ω , ranks (r_1, r_2, r_3) , parameters (λ_1, ρ)

- 1: **Warm start:** $U^{(n)} \leftarrow \text{TruncatedHOSVD}(\mathcal{P}_\Omega(\mathcal{Y}))$
- 2: $\mathcal{E} \leftarrow 0$, $\Lambda \leftarrow 0$
- 3: **repeat**
- 4: Update \mathcal{G} (three tiny ridge systems)
- 5: **for** $n = 1$ **to** 3 **do**
- 6: Update $U^{(n)}$ (one thin SVD)
- 7: **end for**
- 8: $\mathcal{Z} \leftarrow \mathcal{G} \times_1 U^{(1)} \times_2 U^{(2)} \times_3 U^{(3)}$
- 9: $\mathcal{E} \leftarrow \text{SoftThreshold}_{\lambda_1/\rho}(\mathcal{Y}_\Omega - \mathcal{Z}_\Omega - \Lambda)$
- 10: $\Lambda \leftarrow \Lambda + \mathcal{P}_\Omega(\mathcal{Z} + \mathcal{E} - \mathcal{Y})$
- 11: **until** $\|\mathcal{Z} - \mathcal{Z}_{\text{prev}}\|_F / \|\mathcal{Z}_{\text{prev}}\|_F < 10^{-5}$ **or** max iterations
- 12: **return** $(\mathcal{Z}, \mathcal{E})$

G Datasets and Settings

The datasets used in the experiments include SR-CACO-2 and three datasets of *in vivo* cellular volumes.

This SR-CACO-2 dataset contains large image tiles $9k \times 9k$, each composed of 10×10 unique sub-images of Caco-2 epithelial cells. Caco-2 cells serve as a reliable model for studying mitotic spindle orientation and epithelial polarity, and can be easily modified for fluorescence tagging. The dataset includes fixed-cell images labeled with three fluorescent markers: mCherry-Histone H2B (chromatin), GFP-tubulin or E-cadherin (cell structure and membrane), and Survivin (midbody during cell division). It provides over 9,000 real LR-HR patch pairs for each cell type, enabling comprehensive evaluation of SISR models across different magnification levels. The dataset setup and experimental protocols are standardized and detailed in the original work, ensuring reproducibility and relevance to live-cell imaging tasks.

We constructed a comprehensive experimental pipeline using three real-world *in vivo* cellular datasets, acquired from live-cell cultures with Zeiss LSM 980 and Nikon A1R confocal microscopy systems. 3D imaging volumes were processed using Zen Blue and Fiji (ImageJ). To minimize phototoxicity during 4D time-lapse imaging, scanning was performed at 7000 Hz with a water immersion objective, which inevitably introduced challenges such as high noise, low contrast, and anisotropic spatial resolution.

To support quantitative evaluation, we collected three benchmark datasets under varied imaging conditions including standard acquisition, high-speed axial scanning, laser-induced damage, and low-frame-rate capture. These datasets were acquired at elevated laser intensities for observational validation but were excluded from model training. Each sequence was segmented into temporal intervals of 50 frames. Laser intensity compensation along the Z-axis ranged from 1-4% for the 405 nm channel and 15-85% for the 561 nm channel.

We also introduce a new dataset comprising 500 annotated 3D fluorescence volumes (265 unique volumes, totaling 22,830 lateral 2D slices), referred to as UnpairedTrain. These volumes were collected independently from the benchmark datasets and do not include direct high-resolution supervision, making them suitable for weakly- or self-supervised learning schemes in fluorescence microscopy.

For training, we used GFP-labeled membrane-stained fluorescent images as input, excluding ground truth HR images from the optimization target to encourage model generalization. The original 4D image volumes have dimensions of $512 \times 712 \times 94$, optimized for preserving cell viability during acquisition. Training was performed using the Adam optimizer with an initial learning rate of 0.0002 and exponential weight decay (decayed every 100 iterations). All models, including ours and baselines, were trained and evaluated on six NVIDIA A100 GPUs.